Monthly Notices
of the
ROYAL ASTRONOMICAL SOCIETY

MNRAS **429,** 2032–2051 (2013) doi:10.1093/mnras/sts475

Clustering analysis of high-redshift luminous red galaxies in Stripe 82

N. Nikoloudakis,[1]⋆ T. Shanks[1] and U. Sawangwit[1,2]

[1]*Physics Department, University of Durham, South Road, Durham DH1 3LE*
[2]*National Astronomical Research Institute of Thailand, Chiang Mai 50200, Thailand*

Accepted 2012 November 22. Received 2012 November 21; in original form 2012 April 16

ABSTRACT

We present a clustering analysis of luminous red galaxies (LRGs) in Stripe 82 from the Sloan Digital Sky Survey (SDSS). We study the angular two-point autocorrelation function, $w(\theta)$, of a selected sample of over 130 000 LRG candidates via colour-cut selections in *izK* with the *K*-band coverage coming from UKIRT (United Kingdom Infrared Telescope) Infrared Deep Sky Survey (UKIDSS) Large Area Survey (LAS). We have used the cross-correlation technique of Newman to establish the redshift distribution of the LRGs. Cross-correlating them with SDSS quasi-stellar objects (QSOs), MegaZ-LRGs and DEEP Extragalactic Evolutionary Probe 2 (DEEP2) galaxies, implies an average redshift of the LRGs to be $z \approx 1$ with space density, $n_{\rm g} \approx 3.20 \pm 0.16 \times 10^{-4}\,h^3\,{\rm Mpc}^{-3}$. For $\theta \leq 10$ arcmin (corresponding to $\approx 10\,h^{-1}$ Mpc), the LRG $w(\theta)$ significantly deviates from a conventional single power law as noted by previous clustering studies of highly biased and luminous galaxies. A double power law with a break at $r_{\rm b} \approx 2.4\,h^{-1}$ Mpc fits the data better, with best-fitting scale length, $r_{0,1} = 7.63 \pm 0.27\,h^{-1}$ Mpc and slope $\gamma_1 = 2.01 \pm 0.02$ at small scales and $r_{0,2} = 9.92 \pm 0.40\,h^{-1}$ Mpc and $\gamma_2 = 1.64 \pm 0.04$ at large scales. Due to the flat slope at large scales, we find that a standard Λ cold dark matter (ΛCDM) linear model is accepted only at 2–3σ, with the best-fitting bias factor, $b = 2.74 \pm 0.07$. We also fitted the halo occupation distribution (HOD) models to compare our measurements with the predictions of the dark matter clustering. The effective halo mass of Stripe 82 LRGs is estimated as $M_{\rm eff} = 3.3 \pm 0.6 \times 10^{13}\,h^{-1}\,{\rm M}_{\odot}$. But at large scales, the current HOD models did not help explain the power excess in the clustering signal.

We then compare the $w(\theta)$ results to the results of Sawangwit et al. from three samples of photometrically selected LRGs at lower redshifts to measure clustering evolution. We find that a long-lived model may be a poorer fit than at lower redshifts, although this assumes that the Stripe 82 LRGs are luminosity-matched to the $AA\Omega$ LRGs. We find stronger evidence for evolution in the *form* of the $z \approx 1$ LRG correlation function with the above flat two-halo slope maintaining to $s \gtrsim 50\,h^{-1}$ Mpc. Applying the cross-correlation test of Ross et al., we find little evidence that the result is due to systematics. Otherwise, it may represent evidence for primordial non-Gaussianity in the density perturbations at early times, with $f_{\rm NL}^{\rm local} = 90 \pm 30$.

Key words: cosmology: observations – galaxies: evolution-high-redshift – large-scale structure of Universe.

1 INTRODUCTION

The statistical study of the clustering properties of massive galaxies provides important information about their formation and evolution which represent major questions for cosmology and astrophysics. The correlation function of galaxies remains a simple yet powerful tool for implementing such statistical clustering studies (e.g. Peebles 1980).

A lot of interest has been concentrated specifically on measuring the clustering correlation function of luminous red galaxies (LRGs; Eisenstein et al. 2001; see also e.g. Zehavi et al. 2005b; Blake, Collister & Lahav 2008; Ross et al. 2008a; Wake et al. 2008; Sawangwit et al. 2011). LRGs are predominantly red massive early-type galaxies, intrinsically luminous ($\geq 3L^{\star}$) (Eisenstein et al. 2003; Loh & Strauss 2006; Wake et al. 2006) and thought to lie in the most massive dark matter haloes. They are also strongly biased objects (Padmanabhan et al. 2007) and this coupled with their bright luminosity makes their clustering easy to detect out to high redshifts. For linear bias, the form of the LRG correlation function will trace

⋆ E-mail: nikolaos.nikoloudakis@durham.ac.uk

that of the mass but even in this case the rate of correlation function evolution will depend on the bias model (e.g. Fry 1996), which in turn depends on the galaxy formation process.

The passive evolution of the LRG LF and slow evolution of the LRG clustering (Wake et al. 2008; Sawangwit et al. 2011) seen in Sloan Digital Sky Survey (SDSS), 2dF-SDSS LRG and Quasar (2SLAQ) and *AA*Ω Surveys already present a challenge for hierarchical models of galaxy formation as predicted for a cold dark matter (CDM) universe. Since the LRG clustering evolution with redshift has been controversial, a major goal is to use the angular correlation function to test if the slow clustering evolution trend continues out to $z \approx 1$.

The uniformity of the LRG spectral energy distributions (SEDs) with their 4000 Å Ca II H&K break offers the ability to apply a colour–colour selection algorithm for our candidates. This technique has been successfully demonstrated primarily by Eisenstein et al. in SDSS in the analysis of LRG clustering at low redshift and then in 2SLAQ (Cannon et al. 2006) and AAΩ (Ross et al. 2008a) LRG surveys at higher redshifts. For our study, the available deep optical-IR *ugrizJHK* imaging data from the SDSS + UKIRT (United Kingdom Infrared Telescope) Infrared Deep Sky Survey (UKIDSS) LAS/DXS surveys in Stripe 82 will be used. This combination of NIR and deep optical imaging data, on a moderate sample size of area $\sim$200 deg^2, results in a sample of $\approx$130 000 LRG candidates at redshift $z \approx 1$.

The main tool for our clustering analysis will be the two-point angular correlation function, $w(\theta)$, which has been frequently used in the past, usually in cases where detailed redshift information was not known. Hence, selecting Stripe 82 LRGs based on colour–magnitude criteria corresponds to a rough photometric redshift (photo-z) estimation based on the 4000 Å break shifting through the passbands. We shall apply the cross-correlation technique which was introduced by Newman (2008) to measure the redshift distribution, $n(z)$, of our photometrically selected samples. One of the main advantages of $w(\theta)$ is that it only needs the $n(z)$ of the sample and then through Limber's formula (Limber 1953) it can be related to the spatial two-point correlation function (2PCF), $\xi(r)$.

In recent clustering studies, it was noted that the behaviour of $\xi(r)$, which has previously been successfully described by a single power law of the form $\xi(r) = (r/r_0)^{-\gamma}$, significantly deviates from such a power law at $\sim 1\,h^{-1}$ Mpc. The break in the power law can be interpreted in the framework of a halo model, as arising from the transition between small scales (one-halo term) to larger than single halo scales (two-halo term). Currently, our theoretical understanding of how galaxy clustering relates to the underlying dark matter is provided by the halo occupation distribution (HOD) model (see e.g. Jing, Mo & Boerner 1998; Ma & Fry 2000; Peacock & Smith 2000; Seljak 2000; Scoccimarro et al. 2001; Berlind & Weinberg 2002) via dark matter halo bias and halo mass function. Furthermore, the evolution of HOD can also give an insight into how certain galaxy populations evolve over cosmic time (White et al. 2007; Seo, Eisenstein & Zehavi 2008; Wake et al. 2008; Sawangwit et al. 2011).

The outline of this paper is as follows. In Section 2, we briefly describe the SDSS and UKIDSS data used in this paper, while in Section 3 we describe the angular function correlation function estimators and their statistical uncertainties. In Section 4, we estimate the redshift distribution through cross-correlations and then present the correlation results together with their power-law fits, ΛCDM model and a halo model in Section 5. Section 6 is devoted to the interpretation of the clustering evolution. In Section 7, we explore potential systematic errors that might affect the large scale clustering signal. We then argue that, if real, an observed large-scale clustering excess may be due to the scale-dependent bias caused by primordial non-Gaussianity and compare our results to other previous works in Section 8. Finally, in Section 9 we summarize and conclude our findings.

Throughout this paper, we use a flat Λ-dominated cosmology with $\Omega_{\rm m} = 0.27$, $H_0 = 100\,h\,{\rm km\,s^{-1}\,Mpc^{-1}}$, $h = 0.7$, $\sigma_8 = 0.8$ and magnitudes are given in the AB system unless otherwise stated.

2 DATA

2.1 LRG sample selection

We perform a *K*-band selection of high-redshift LRGs in Stripe 82 based on the combined optical and IR imaging data, *ugrizJHK*, from SDSS DR7 (Abazajian et al. 2009) and UKIDSS LAS surveys (Lawrence et al. 2007; Warren et al. 2007), respectively. In previous studies, *gri* and *riz* colours have been used to select low- to medium-redshift LRGs, such as SDSS (Eisenstein et al. 2001), 2SLAQ (Cannon et al. 2006) and AAΩ (Ross et al. 2008a) LRGs surveys up to $z \approx 0.7$. In this work we aim to study LRGs at $z \approx 1$, thus we use the *izK* colour–magnitude limits for our selection in order to sample the 4000 Å Ca II H&K break of the LRGs' SED as it moves across the photometric filters (Fukugita et al. 1996; Smith et al. 2002) taking advantage of the NIR photometry coverage from UKIDSS LAS. Coupling the UKIDSS LAS to $K_{\rm Vega} \leq 18$ with the SDSS *ugriz* imaging to $i_{AB} < 22.5$ in Stripe 82 produces an unrivalled combination of survey area and depth. Our selection criteria are as follows.

SDSS Best Imaging

$$
\begin{aligned}
&z - K + 0.9(i - z) \geq 1.8, \ \text{Pri A} \sim 700\,{\rm deg^{-2}}\\
&z - K + 0.9(i - z) \geq 2.3, \ \text{Pri B} \sim 240\,{\rm deg^{-2}}\\
&z - K - 0.9(i - z) \geq -0.2\\
&-0.5 \leq i - z \leq 1.7\\
&z - K \leq 4.0\\
&17.0 \leq K \leq 18\\
&z \leq 22.0. \qquad (1)
\end{aligned}
$$

The photometric selection of LRGs at $z > 1$ requires a combination of optical and NIR photometry as the 4000 Å band straddles the z band. The selection of high-redshift LRGs is done on the basis of SDSS *iz* photometric data and the LAS *K*-band data (Fig. 1). LRG evolutionary models of Bruzual & Charlot (2003) are overplotted for single burst and $\tau = 1$ Gyr galaxy models indicating the *izk* plane area where we should apply our selections in order to study the high-z LRG candidates.

Late-type star contamination is a major problem in selecting a photometric sample of $z \approx 1$ LRGs. Here the $z - K$ colour also helps to distinguish the M stars colour locus from those of galaxies. From Fig. 1, we see that most of the M stars lie at the bottom of the *izK* colour plane. We identify these M stars by assuming their typical NIR colour, $J - K < 1.3$. However, this means that our selection criteria must involve *J*-band data and would reduce the sky coverage due to the data availability. Therefore we choose to exclude these M stars by applying a cut in *izK* colour plane with the condition $z - K - 0.9(i - z) \geq -0.2$ in equation (1).

All magnitudes and colours are given in SDSS *AB* system and are corrected for extinction using the Galactic dust map of Schlegel, Finkbeiner & Davis (1998). All colours described below refer to the differences in 'model' magnitudes (see Lupton et al. 2001, for a review on model magnitudes) unless otherwise stated.

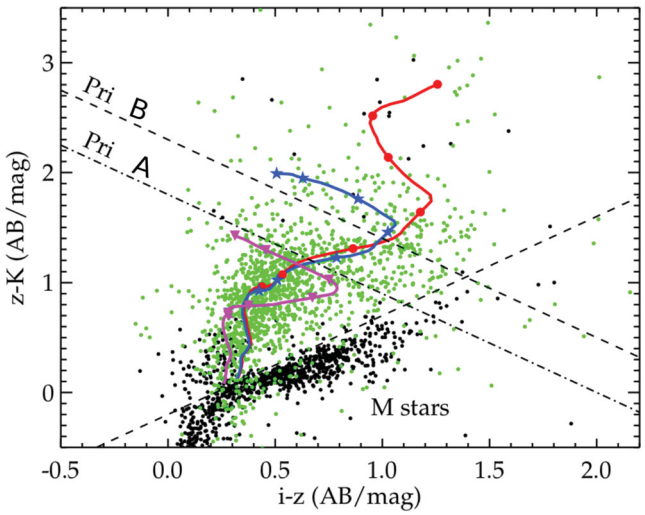

Figure 1. iz versus zK colour–colour plot. Priority A and B correspond to the $\sim$700 deg^{-2} and $\sim$240 deg^{-2} LRG samples, respectively. Objects with $J-K<1.3$ which is typical for M stars are plotted as black circles whereas those with $J-K\geq 1.3$ are plotted in green. Evolutionary tracks for single burst (red line) and $\tau=1$ Gyr (blue line) are overplotted from $z=0$ to 1.6 with symbols indicating z interval of 0.2. The evolutionary track of late-type galaxies (magenta line) is also shown for comparison.

Applying the above selection criteria (equation 1) on the SDSS DR7, we have two main LRG samples with a total observed area (after masking) of $\approx$200 deg^2. The first sample has 130 819 LRG candidates with a sky surface density of $\approx$700 deg^{-2} and the second one 44 543 with a sky density of $\approx$240 deg^{-2}. The 240 deg^{-2} LRG sample was selected in such a way to check if the redshift distribution implied by cross-correlations is higher than the 700 deg^{-2} LRG sample.

3 THE TWO-POINT ANGULAR CORRELATION FUNCTION MEASUREMENTS AND ERRORS

3.1 $w(\theta)$ estimators

The probability of finding a galaxy within a solid angle $\delta\Omega$ on the celestial plane of the sky at a distance θ from a randomly chosen object is given by (e.g. Peebles 1980)

$$\delta P = n[1+w(\theta)]\delta\Omega, \tag{2}$$

where n is the mean number of objects per unit solid angle. The angular 2PCF in our case actually calculates the excess probability of finding a galaxy compared to a uniform random point process.

Different estimators can be used to calculate $w(\theta)$, so to start with we use the minimum variance estimator from Landy & Szalay (1993),

$$w_{\rm LS}(\theta)=1+\left(\frac{N_{\rm rd}(N_{\rm rd}-1)}{N(N-1)}\right)\frac{DD(\theta)}{RR(\theta)}-2\left(\frac{N_{\rm rd}}{N}\right)\frac{DR(\theta)}{RR(\theta)} \tag{3}$$

where $DD(\theta)$ is the number of LRG–LRG pairs, $DR(\theta)$ and $RR(\theta)$ are the numbers of LRG–random and random–random pairs, respectively, with angular separation θ summed over the entire survey area. $N_{\rm rd}$ is the total number of random points, N is the total number of LRGs and $N_{\rm rd}/N$ is the normalization factor. For our calculation we used two LRG samples (as explained in Section 2.1) with different sky density; thus the density of the random catalogue that we use is $\sim$20 times and $\sim$60 times the number of the real galaxies for the first and second LRG samples, respectively. Using a high number density random catalogue helps to ensure the extra shot noise is reduced as much as possible.

We also compute $w(\theta)$ by using the Hamilton (1993) estimator which does not depend on any normalization and is given by

$$w_{HM}(\theta)=\frac{DD(\theta)\cdot RR(\theta)}{DR(\theta)^2}-1. \tag{4}$$

The Landy–Szalay estimator when used with our samples gives negligibly different results to the Hamilton estimator. Note that the Landy–Szalay estimator is used throughout this work except in Section 7.1 where we used both estimators to test for any possible gradient in number density of our samples.

For the computation of the cross-correlations in Sections 4 and 7 we use the estimator (Guo, Zehavi & Zheng 2011):

$$w_{\rm cross}(\theta)=\frac{D_{\rm G}D_{\rm S}(\theta)-D_{\rm G}R_{\rm S}(\theta)-D_{\rm S}RD(\theta)-R_{\rm G}R_{\rm S}(\theta)}{R_{\rm G}R_{\rm S}(\theta)} \tag{5}$$

where the subscript G and S stands for the contribution in the pairs of the quantities that are cross-correlated in each case.

3.2 Error estimators

To determine statistical uncertainties in our methods, we used three different methods to estimate the errors on our measurements. First, we calculated the error on $w(\theta)$ by using the Poisson estimate

$$\sigma_{\rm Poi}=\frac{1+w(\theta)}{\sqrt{DD(\theta)}}. \tag{6}$$

Secondly, we used the field-to-field error which is given by

$$\sigma^2_{\rm FtF}(\theta)=\frac{1}{N-1}\sum_{i=1}^{N}\frac{DR_i(\theta)}{DR(\theta)}[w_i(\theta)-w(\theta)]^2, \tag{7}$$

where N is the total number of subfields, $w_i(\theta)$ is an angular correlation function estimated from the ith subfield and $w(\theta)$ is measured using the entire field. For this method we divide our main sample to 36 subfields of equal size, $\sim$6 deg^2. We also reduce the number of subfields down to 18 with sizes of $\sim$12 deg^2 as we want to test how the results could deviate by using different sets of subsamples. While Stripe 82 has only $\sim 2\overset{\circ}{.}5$ height, our subfields with their $\sim 2\overset{\circ}{.}5$ and $\sim 5^\circ$ widths are a reasonable size for estimating the correlation function up to scales of 1°–2°.

Our final method is jackknife resampling, which is actually a bootstrap method. This technique has been widely used in clustering analysis studies with correlation functions (see e.g. Scranton et al. 2002; Zehavi et al. 2005a; Ross et al. 2007; Norberg et al. 2009; Sawangwit et al. 2011). The jackknife errors are computed using the deviation of the $w(\theta)$ measured from the combined 35 subfields out of the 36 subfields (or 17 out of 18 when 18 subfields are used). The subfields are the same as used for the estimation of the *field-to-field* error above. $w(\theta)$ is calculated repeatedly, each time leaving out a different subfield and hence results in a total 36 (or 18) measurements. The jackknife error is then

$$\sigma^2_{\rm JK}(\theta)=\sum_{i'=1}^{N}\frac{DR_{i'}(\theta)}{DR(\theta)}[w_{i'}(\theta)-w(\theta)]^2, \tag{8}$$

where $w_{i'}(\theta)$ is a measurement using the whole sample except the ith subfield and $DR_{i'}(\theta)/DR(\theta)$ is approximately 35/36 (or 17/18) with slight variation depending on the size of resampling field. A comparison of the error estimators can be seen in Fig. 2. Poisson errors are found to be much smaller compared to jackknife errors

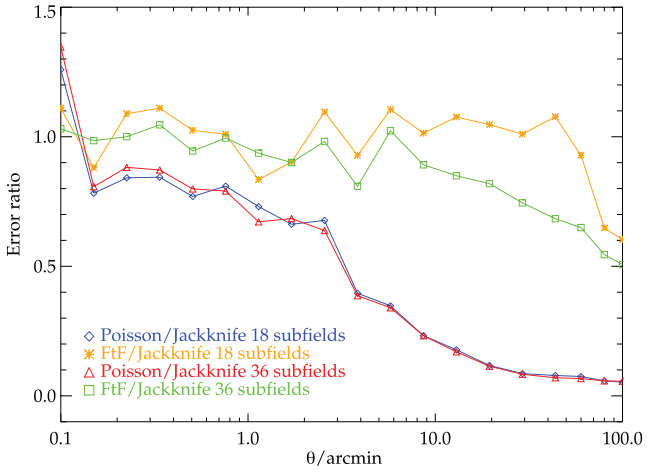

Figure 2. Comparison of the measured error ratios of the Jackknife, field-to-field and the Poisson errors for the $w(\theta)$ measurements of the 700 deg^{-2} Stripe 82 LRG sample. Two different resampling sets have been used for the Jackknife and field-to-field errors: the first one based on 36 subfields and the second from 18 subfields.

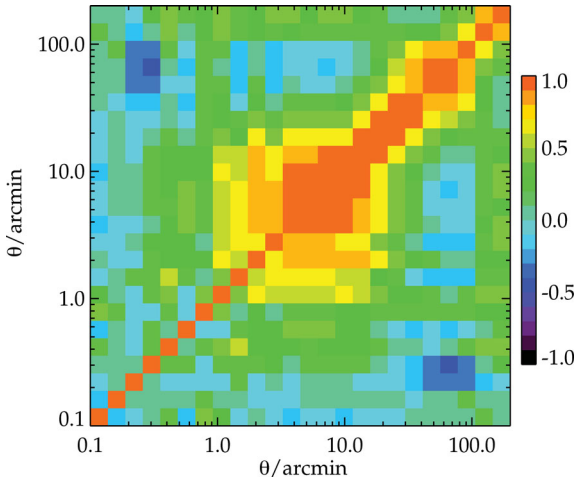

Figure 3. The correlation coefficients $\mathbf{r}_{ij}$, showing the level of correlation between each angular separation bin for the 700 deg^{-2} Stripe 82 LRG sample as calculated by using 36 subfields.

particularly at larger scales. Field-to-field errors give similar results as jackknife errors, except at $\theta \gtrsim 10$ arcmin where the FtF errors underestimate the true error due to missing cross-field pairs. Since the jackknife errors are better at a scale of the order of 100 arcmin which are of prime interest here, these are the error estimators that will be used in this work unless otherwise stated.

When calculated in small survey areas, $w(\theta)$ can be affected be an 'integral constraint', *ic*. Normally $w(\theta)$ has a positive signal at small scales and if the surveyed area is sufficiently small, this will cause a negative bias in $w(\theta)$ at largest scales (Groth & Peebles 1977), i.e. $w_{est}(\theta) = w(\theta) - ic$. The integral constraint can be calculated from (see e.g. Roche & Eales 1999)

$$ic = \frac{\sum RR(\theta) w_{\rm model}(\theta)}{\sum RR(\theta)}, \tag{9}$$

where for the $w_{\rm model}(\theta)$ we assume the standard ΛCDM model in the linear regime (Section 5.3). No integral constraint is initially applied to our full sample results as the expected magnitude of *ic* is smaller than the $w(\theta)$ amplitudes at scales analysed in this paper. This position will be reviewed when we move on to discuss models with excess power at large scales in Section 7.

To provide robust and accurate results from the correlation functions, we are also interested in model fitting to the observed $w(\theta)$ (see in Sections 5.2, 5.3 and 5.4). Hence, for model fitting we will use the covariance matrix, which is calculated by

$$\mathbf{C}_{ij} = \frac{N-1}{N} \sum_{i,j=1}^{N} \left[w(\theta_i) - \overline{w(\theta_i)}\right] \left[w(\theta_j) - \overline{w(\theta_j)}\right] \tag{10}$$

where the $w_i(\theta_i)$ is the correlation function measurement value excluding the ith subsample and the factor $N-1$ corrects from the fact that the realizations are not independent (Myers et al. 2007; Norberg et al. 2009; Ross, Percival & Brunner 2010; Crocce et al. 2011; Sawangwit et al. 2011). The jackknife errors are the square root of the diagonal elements of the covariance matrix, so we can now calculate the correlation coefficient, which is defined in terms of the covariance,

$$\mathbf{r}_{ij} = \frac{\mathbf{C}_{ij}}{\sqrt{\mathbf{C}_{ii} \cdot \mathbf{C}_{jj}}} \tag{11}$$

where $\sigma_i^2 = C_{ii}$ (see Fig. 3). We can see that the bins are strongly correlated at large scales. The covariance matrix is more stable when we use 36 Jackknife subfields instead of 18, so we will use only the covariance matrix for the case of 36 subfields.

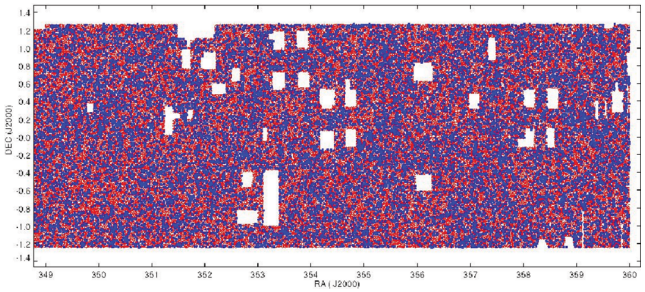

Figure 4. A fraction of the total ∼200 deg^2 observed area in Stripe 82. LRG candidates (red) and random objects (blue) follow the same angular selection. Empty sky patches resulting from the lack of *K*-band coverage in the combined optical-IR data.

3.3 Angular mask and random catalogue

To measure the observed angular correlation function we must compare the actual galaxy distribution with a catalogue of randomly distributed points. The random catalogue must follow the same geometry as the real galaxy catalogue, so for this reason we apply the same angular mask. The mask is constructed from 'BEST' DR7 imaging sky coverage.[1] Furthermore, regions excluded in the quality holes defined as 'BLEEDING', 'TRAIL', 'BRIGHT_STAR' and 'HOLE'. The majority of the holes in the angular mask is from the lack of *K* coverage in Stripe 82. The final mask is applied to both our data and random catalogue (see Fig. 4).

For generating the randomly distributed galaxies/points, we tried two different ways in order to modulate the surface density of the random points to follow the number density and the selection function of the real data. The selection function of the random catalogue mimics only the angular selection of the real data.

For the first method, we use a uniform density for the random points across the Stripe 82 area, so the normalization factor, $N_{\rm rd}/N$, would be ∼20 and ∼60 for the 700 deg^{-2} and the 240 deg^{-2} LRG

[1] http://www.sdss.org/dr7

samples, respectively. A second random catalogue was created by dividing Stripe 82 into six smaller subfields ($15 \times 2.5\,\mathrm{deg}^2$ each) and normalizing the density of random points to the density of galaxies within each subfield. The difference between the measured angular correlation function when we use the 'global' or the 'local' random catalogue is negligible. We will use the 'global' random catalogue for the clustering analysis. A *k*d-trees code (Moore et al. 2001) has been used to minimize the computation time required in the pair counting procedure.

4 LRG *N(z)* VIA CROSS-CORRELATIONS

Even if the redshift of individual galaxies is not available, the 3D clustering information can yet be recovered if the sample's redshift distribution, *n(z)*, is known. This can be achieved using Limber's inversion equation (Limber 1953) which can project the spatial galaxy correlation function, $\xi(r)$, to the angular correlation function given the *n(z)* of the sample:

$$w(\theta) = 2\int_0^\infty \mathrm{d}x f(x)^2 \int_0^\infty \mathrm{d}u\ \xi\left(r = \left(u^2 + x^2\theta^2\right)^{1/2}\right), \qquad (12)$$

where *f(x)* is the galaxy redshift selection function. For our photometric selected LRG samples, only a very small fraction has a measured redshift, thus it is vital to estimate the *n(z)* of the Stripe 82 LRG samples.

One method for estimating the redshift distribution of the sample could be based on the various popular programs that derive photometric redshifts (photo-*z*'s). Photo-*z* estimates are based on the deep multi-band photometry coverage, and work by tracing some specific spectral features across the combination of filters which are then compared with different types of SED templates. Indeed, our *izK* selection is a rough photo-*z* cut as we follow the movement of the 4000 Å break across the selected bands. In order to use the angular correlation function and the information that is encoded we need the *n(z)* of our sample, hence we follow the technique of Newman (2008) for reconstructing the LRG redshift distribution from cross-correlations.

4.1 Redshift distribution reconstruction

We employ Newman's method, which is about determining the underlying redshift distribution of a sample of objects (LRGs in our case) through cross-correlation with a sample of known redshift distribution. By cross-correlating the sample (or samples) with known redshift and the sample under consideration, if both samples lie at the same distance, this will give a strong clustering signal. If the two samples that we are cross-correlating are separated and are at different *z* distances, no cross-correlation signal will result. Thus, through the cross-correlations we can infer our photometrically selected LRG sample *z* ranges.

Following Newman (2008) the probability distribution function of the redshift of the Stripe 82 LRG samples, $\phi_\mathrm{p}(z)$, is

$$\phi_\mathrm{p}(z) = w(z)\frac{3-\gamma}{2\pi}\frac{d_\mathrm{A}(z)^2 dl/dz}{H(\gamma) r_{0,\mathrm{sp}}^{\gamma} r_{\mathrm{max}}^{3-\gamma}} \qquad (13)$$

where $w(z)$ is the integrated cross-correlation function, $w_\mathrm{sp}(\theta, z)$, of the LRG photometric samples with the samples of known spectroscopic redshift (see Section 4.2), $H(\gamma) = \Gamma(1/2)\Gamma((\gamma - 1)/2)/\Gamma(\gamma/2)$ where $\Gamma(\chi)$ is the Gamma function, d_A is the comoving angular distance and *dl* is the comoving distance at redshift *z*. The comoving distance r_max corresponds to the maximum angle at given redshift, which must be large enough to avoid non-linear biasing effects.

To derive $\phi_\mathrm{p}(z)$ via equation (13) we must estimate $w_\mathrm{sp}(\theta, z) \sim \phi_\mathrm{p}(z)\, r_{0,\mathrm{sp}}^{\gamma_\mathrm{sp}}$, since the angular size distance, $d_\mathrm{A}(z)$, and the comoving distance, $l(z)$, are given by the assumed cosmology. Thus we now require only the knowledge of the γ_sp and $r_{0,\mathrm{sp}}$ parameters as a function of redshift. Fortunately, under the assumption of linear biasing, the cross-correlation of the two samples under consideration is the result of the geometric mean of the autocorrelation functions of the samples, i.e. $\xi_\mathrm{sp} = (\xi_{ss}\xi_{pp})^{\frac{1}{2}}$, hence we can use the information provided by autocorrelation measurements for each sample to break the degeneracy between correlation strength and redshift distribution.

Newman investigates the effect of systematics such as: different cosmologies, bias evolution, errors from the autocorrelation measurements and field-to-field zero-points variations in the final redshift probability distribution result. These issues could be more important in the case of future photometric surveys aimed at placing constraints on the equation of dark energy.

4.2 Cross-correlation data sets

Newman's angular cross-correlation technique requires the use of a data sample with known spectroscopic, or sufficiently accurate photometric, redshifts. For this reason we use a variety of samples with confirmed spectroscopic and photometric redshifts for the cross-correlations with Stripe 82 LRGs. The data samples that we use are: DEEP2 DR3 galaxies (Davis et al. 2003, 2007), MegaZ-LRGs (Collister et al. 2007), SDSS DR6 quasi-stellar object (QSOs; Richards et al. 2009) and SDSS DR7 QSOs (Schneider et al. 2010). In Fig. 5 we show the normalized redshift distributions of all the samples and in Table 1 we present the number of objects in each redshift bin.

By using the above data sets for cross-correlation we satisfy the principal requirements of Newman's method, with the most important being that the sky coverage of the data sets must overlap the Stripe 82 LRGs. It must be mentioned though that not all the redshift surveys have the same sky coverage as Stripe 82 LRGs, so we reconstruct two redshift distributions via the cross-correlations providing us with the opportunity to check how much the *n(z)*

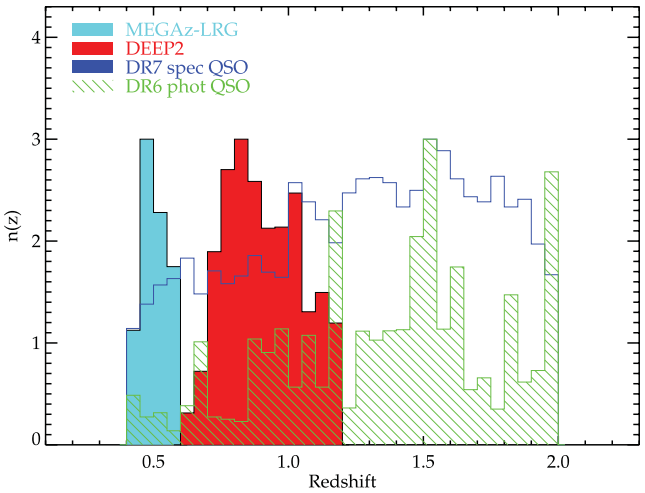

Figure 5. Normalized redshift distributions of MegaZ-LRGs, DEEP2 galaxies and SDSS QSOs in Stripe 82 that are used in cross-correlations with the LRG samples.

Table 1. Number of objects in each separate redshift bin used for the cross-correlations with Stripe 82 LRGs.

	Sample			
Redshift	DEEP2	MegaZ-LRGs	DR6 photometric sample	DR7 spectroscopic sample
0.4–0.6	–	30 503	436	456
0.6–0.8	3152	–	695	526
0.8–1.0	5512	–	1199	547
1.0–1.2	3620	–	1630	729
1.2–1.4	–	–	1312	820
1.4–1.6	–	–	2646	854
1.6–1.8	–	–	1193	803
1.8–2.0	–	–	1990	668

cross-correlation technique is affected by area selection. One $n(z)$ is reconstructed by using all the data sets, and the other $n(z)$ by using only SDSS QSOs in the cross-correlations.

4.2.1 *SDSS DR6 and DR7 QSOs*

QSO surveys are the main samples that we used for our cross-correlation measurements and they span the redshift range $0.4 \leq z \leq 2.0$. When we refer to QSO data sets, we separate them into spectroscopic and photometric samples.

For the spectroscopic QSO sample we use the fifth edition of the SDSS Quasar Catalogue, which is based on the SDSS DR7 (Schneider et al. 2010). The original data set contains 105 783 spectroscopically confirmed QSOs, from which only 5403 in Stripe 82 have been used at $0.4 \leq z \leq 2.0$ for cross-correlations (Table 1) with $i < 22$ (∼28 per cent of QSOs at $i > 20$).

The photometric QSO sample comes from the photometric imaging data of the SDSS DR6 (Richards et al. 2009). The parent catalogue contains ∼1000 000 QSOs candidates from which we use 11 101 with $i < 21.3$ in Stripe 82 and in the same redshift range as the spectroscopic QSOs.

In Fig. 6 we plot the cross-correlations between the Stripe 82 LRGs and the SDSS QSOs. We show only the case for cross-correlations of the 700 deg^{-2} Stripe 82 LRG sample with the spectroscopic and photometric SDSS QSOs. Cross-correlation with the 240 deg^{-2} LRG sample does not differ much. Errors shown here and for the other cross-correlation cases are jackknife errors.

4.2.2 *DEEP2 Sample*

The next sample of galaxies that we use is DEEP2 DR3 galaxies (Davis et al. 2003, 2007). The survey coverage in Stripe 82 is ∼1.7 deg^2 with $i < 24$. Galaxies in DEEP2 are split in three redshift bins with 0.2 step in the redshift range $0.6 \leq z \leq 1.2$. The redshift distribution of the DEEP2 DR3 sample is shown in Fig. 5, with 12 284 galaxies in total. In Fig. 7 we show the results of the cross-correlations of the 700 deg^{-2} and 240 deg^{-2} LRG samples with the DEEP2 galaxies in the three aforementioned redshift bins.

4.2.3 *MegaZ-LRG sample*

The last sample that we use are LRGs from the MegaZ-LRG photometric catalogue (Collister et al. 2007). MegaZ-LRGs are used only in the redshift range of $0.4 \leq z \leq 0.6$ with $i < 20$. This sample offers us the ability to check the clustering properties of our high-redshift LRG candidates with another sample of LRGs. The total number of MegaZ-LRGs that we use for cross-correlations is 30 503. In Fig. 8 the cross-correlations between the Stripe 82 LRGs and the MegaZ-LRGs are shown.

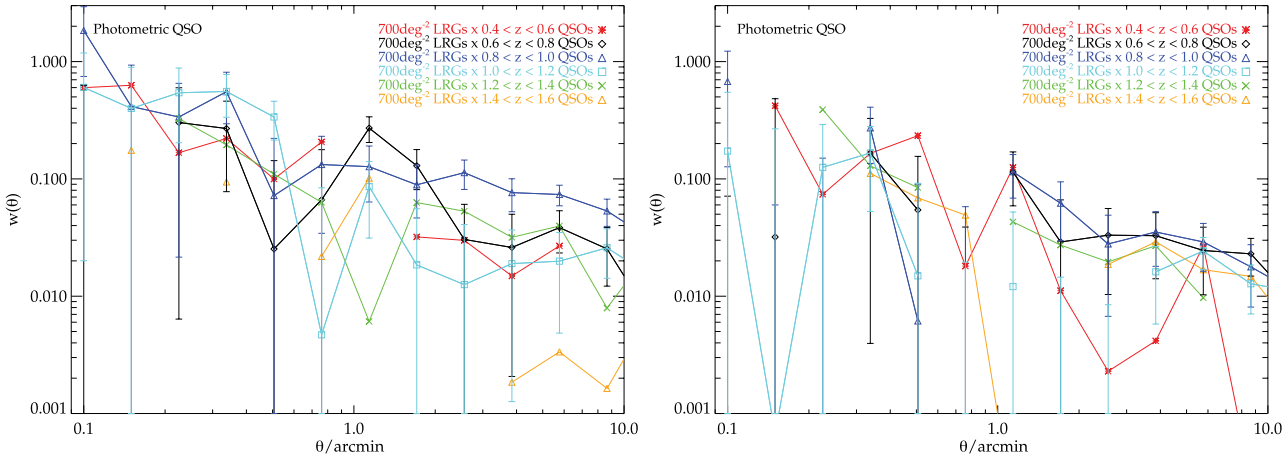

Figure 6. (a) Cross-correlation measurements of the 700 deg^{-2} Stripe 82 LRG sample with spectroscopic SDSS QSOs. (b) Same as (a) but now photometric SDSS QSOs are involved in the cross-correlations. Measurement uncertainties are 1σ jackknife errors.

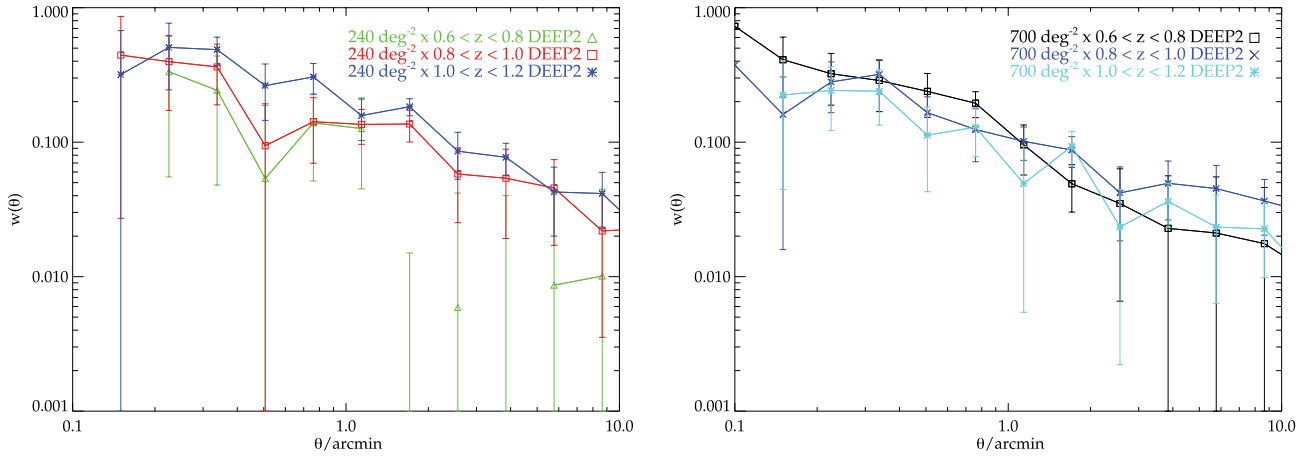

Figure 7. Cross-correlation measurements of the 240 deg^{-2} and 700 deg^{-2} Stripe 82 LRG samples with DEEP2 galaxies in (a) and (b), respectively. Uncertainties are 1σ jackknife errors.

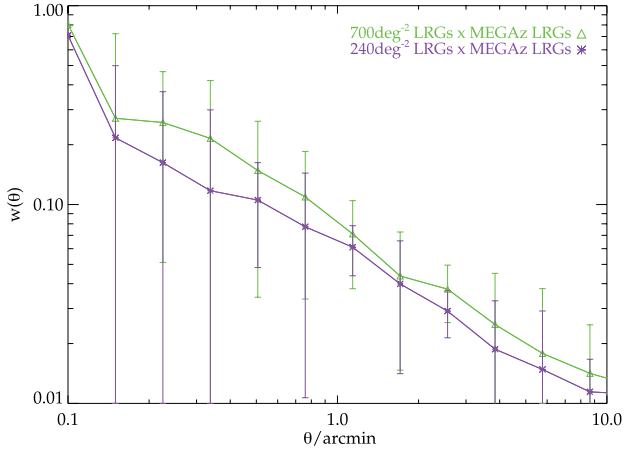

Figure 8. Cross-correlation measurements of the 700 deg^{-2} (green diamond) and 240 deg^{-2} (purple star) Stripe 82 LRGs with MegaZ-LRGs, along with 1σ jackknife errors.

4.3 Cross-correlation results for $n(z)$

Having estimated the clustering signal from the cross-correlations of the above samples, we proceed to the reconstruction of the redshift distribution of the photometrically selected Stripe 82 LRG candidates. To estimate the probability distribution function of the redshift, $\phi_{\rm p}(z)$, for the high-z LRG candidates we use equation (13). The pair-weighted clustering signal of the cross-correlations has been integrated up to ≈6 arcmin for each redshift bin.

In Fig. 9 we can see the two cases of the estimated probability distribution function of the redshift for the high-z LRG candidates. For the first case, $\phi_{\rm p}(z)$ has been estimated by using the spectroscopic SDSS QSOs whereas in the other case, $\phi_{\rm p}(z)$ is estimated using only the photometric SDSS QSOs (DEEP2 galaxies and MegaZ-LRGs are also always used). For both cases we plot the errors estimated for each point in the redshift bin from the contributed cross-correlated sample.

To estimate the redshift distribution, $n(z)$, we use the weighted mean for the $\phi_{\rm p}(z)$ in each redshift bin, calculated through

$$n(z) = \frac{\sum_{i=1}^{k}(\phi_{\rm p}(i)/\sigma_i^2)}{\sum_{i=1}^{k}(1/\sigma_i^2)}, \qquad (14)$$

where k is the total number of bins at that redshift, $\phi_{\rm p}(i)$ is the measured probability distribution function of each cross-correlation data set in the ith bin and σ_i is the error on that measurement.

The spectroscopic QSO $\phi_{\rm p}(z)$ in Fig. 9(a) compared to the photo-z case in Fig. 9(b) gives increased probability at $z \sim 1$. This may be explained by the SDSS QSO spectroscopic redshifts being more precise. For this reason, in our analysis and in fitting models to our $w(\theta)$ results, we will use only the spectroscopic $n(z)$ for higher accuracy.

In Fig. 10 we plot the normalized redshift distribution of the 240 deg^{-2} and 700 deg^{-2} LRGs samples as calculated from equations (13) and (14). When we selected the two LRG samples from the *izK* colour-plane, we applied a redder selection for the 240 deg^{-2} sample (see equation 1), aiming for a sample with a slightly higher redshift peak in the distribution as predicted from the evolutionary tracks in Fig. 1. This small difference may be seen between the spectroscopic $n(z)$ of the 700 deg^{-2} and 240 deg^{-2} samples where the bluer cut has an average of $z \sim 1$ where for the redder sample the average is $z \sim 1.1$. But since the 700 deg^{-2} LRG sample has higher statistical accuracy in the $n(z)$ determination, the majority of our analysis will be focused in this sample.

5 RESULTS

5.1 Measured $w(\theta)$ and comparisons

In Fig. 11 we compare the observed angular correlation function of the 700 deg^{-2} LRG in Stripe 82 with Sawangwit et al. (2011) results. The $w(\theta)$ measurements are presented with 1σ Jackknife errors.

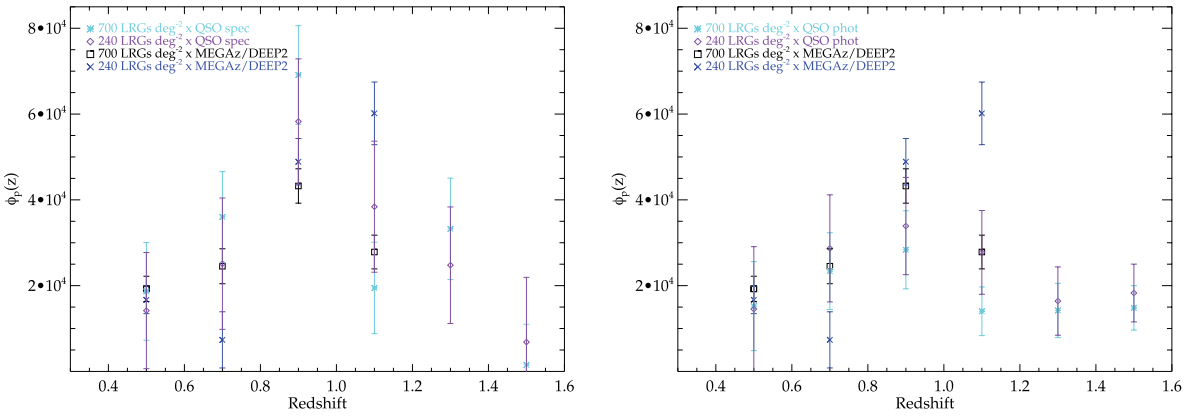

Figure 9. (a) The probability distribution function of the redshift, $\phi_p(z)$, of the 700 deg^{-2} and 240 deg^{-2} Stripe 82 LRGs as estimated through cross-correlations with MegaZ-LRGs, DEEP2 galaxies and spectroscopic SDSS QSOs. (b) Same as in (a) but now using photometric SDSS QSOs instead of spectroscopic in the cross-correlations. Error bars shown in both cases are 1σ jackknife summed up to 6 arcmin.

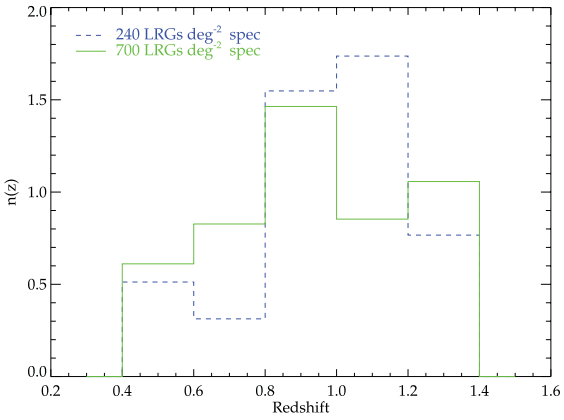

Figure 10. Weighted normalized redshift distribution of the Stripe 82 LRGs candidate samples when we use the spectroscopic SDSS QSOs along with the DEEP2 and MegaZ-LRG data sets. As expected the 700 deg^{-2} sample (solid green line) $n(z)$ peak is lower when compared with the 240 deg^{-2} sample (dashed blue line).

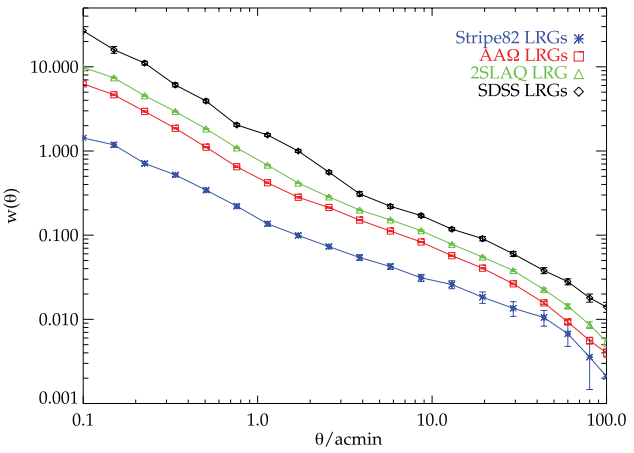

Figure 11. The angular correlation function, $w(\theta)$, from the 700 deg^{-2} Stripe 82 LRGs (star), AAΩ LRGs (square), 2SLAQ LRGs (triangle) and SDSS LRGs (diamond). At small scales all of the measurements show similar clustering behaviour, but at large scales the Stripe 82 clustering slope appears to be flatter than the lower z samples.

The work of Sawangwit et al. involved three LRG data sets at $z \leq 1$:

(i) SDSS LRGs at $z \sim 0.35$
(ii) 2SLAQ LRGs $z \sim 0.55$
(iii) AAΩ LRGs $z \sim 0.68$.

From Fig. 11 we can see that at small scales, $\theta \lesssim 1$ arcmin, the clustering trend for all the samples is similar but with decreasing amplitude for increasing redshift. At larger scales, we note that the $w(\theta)$ of the Stripe 82 LRGs seems to have a flatter slope than the other samples, departing from the expected behaviour for the correlation function.

Further comparisons below with the LRG clustering results of Sawangwit et al. will focus on the slope and amplitude of the $w(\theta)$ results, with an initial view to interpret any changes in terms of evolution. It is therefore of interest to see how the Stripe 82 sample matches to the LRG samples used in previous studies in terms of luminosity and comoving space density.

A pair-weighted galaxy number density is given by (see e.g. Ross, Brunner & Myers 2008b)

$$n_g = \int \mathrm{d}z \frac{H(z)n(z)}{\Omega_{\rm obs}\, cl^2(z)} \times n^2(z) \Big/ \int \mathrm{d}z n^2(z), \qquad (15)$$

where $\Omega_{\rm obs}$ is the observed area of the sky, $l(z)$ is the comoving distance to redshift z and c is the speed of light. The observed space density for the 700 deg^{-2} Stripe 82 sample is found to be $\approx 3.20 \pm 0.16 \times 10^{-4}\, h^3\, \mathrm{Mpc}^{-3}$. The quoted 1σ error has been estimated from the difference of the number density as calculated through equation (15) and by converting Fig. 10 into a plot of number density as a function of z (by dividing its bin by its corresponding volume).

Within the uncertainties of our $n(z)$, the 700 deg^{-2} sample appears to have similar space density to that of the AAΩ LRG sample (see Table 2 in Section 5.2). However, in this study we do not yet have redshift information for individual LRGs, not even for a subset of the sample. Hence it is more uncertain if our sample has similar luminosity as the LRG samples used by Sawangwit et al. (2011). We therefore take the fact that the samples are number density matched to imply that they are also approximately luminosity matched which may turn out to be a reasonable assumption (see e.g. Sawangwit et al. 2011). This then should enable us to compare the clustering slopes

Table 2. Best-fitting parameters for the single and double power-law fits to the angular correlation function.

Sample	$\bar{z}$	n_g (h^3 Mpc^{-3})	Single power law			Double power law			
			γ	$r_0(h^{-1}$ Mpc)	χ^2_{red}	$\gamma_{1,2}$	$r_{0,1,2}(h^{-1}$ Mpc)	$r_b(h^{-1}$ Mpc)	χ^2_{red}
AAΩ LRGs	0.68	2.7×10^{-4}	1.96 ± 0.01	7.56 ± 0.03	42.8	2.14 ± 0.01	5.96 ± 0.03	1.3	3.4
(110 deg^{-2})						1.81 ± 0.02	7.84 ± 0.04		
Stripe 82 LRGs	1.0	$3.20 \pm 0.16 \times 10^{-4}$	2.01 ± 0.01	7.54 ± 0.16	5.89	2.01 ± 0.02	7.63 ± 0.27	2.38	3.65
(700 deg^{-2})						1.64 ± 0.04	9.92 ± 0.40		

and amplitudes of the AAΩ and Stripe 82 and infer any evolution independently of luminosity dependence.

5.2 $w(\theta)$ and power-law fits

Our first aim here is to fit power laws to the Stripe 82 $w(\theta)$ to provide a simple parametrization of the results. Our second aim is to make comparisons of the 3D correlation amplitudes and slopes to measure evolution. Both aims will require application of Limber's formula to relate the 2D and 3D correlation functions.

We begin by noting that the simplest function fitted to correlation functions is a single power law with amplitude r_0 and slope γ. In previous studies, the spatial correlation function has been frequently described by a power law of the form

$$\xi(r) = \left(\frac{r}{r_0}\right)^{-\gamma}. \quad (16)$$

The angular correlation function as a projection of $\xi(r)$ can be written as $w(\theta) = \alpha\theta^{1-\gamma}$, commonly with a slope fixed at $\gamma = 1.8$. The amplitude of the angular correlation function, α, can be related with the correlation length r_0 through Limber's formula (equation 12) using the equation (Blake et al. 2008):

$$\alpha = C_\gamma\, r_0^\gamma \int \mathrm{d}z\, n(z)^2 \left(\frac{\mathrm{d}x}{\mathrm{d}z}\right)^{-1} x(z)^{1-\gamma}, \quad (17)$$

where $n(z)$ is the redshift distribution, $x(z)$ is the comoving radial coordinate at redshift z and the numerical factor $C_\gamma = \Gamma(\frac{1}{2})\Gamma(\frac{\gamma}{2} - \frac{1}{2})/\Gamma(\frac{\gamma}{2})$.

A deviation from a single power law at $\sim 1\,h^{-1}$ Mpc has been measured in previous studies (Shanks et al. 1983; Blake et al. 2008; Ross et al. 2008a; Kim et al. 2011; Sawangwit et al. 2011) and can be explained by the one- and two-halo terms imprinted in the clustering signal under the assumption of the halo model (see Section 5.4). To parametrize the clustering characteristics of our sample, we fit a single power law and a double power law to our measured angular correlation function. The double power-law form is given as

$$w_1(\theta) = \left(\frac{\theta}{\theta_{0,1}}\right)^{1-\gamma_1} \quad (\theta < \theta_b) \quad (18)$$

$$w_2(\theta) = \left(\frac{\theta}{\theta_{0,2}}\right)^{1-\gamma_2} \quad (\theta \geq \theta_b) \quad (19)$$

with θ_b to be the break point at $\approx$1.2 arcmin where the power-law slope changes from being steeper at small scales (<1.2 arcmin) to flatter at large scales.

The power laws are fitted in the range $0.1 < \theta < 30$ arcmin using the χ^2-minimization with the full covariance matrix constructed from the jackknife resampling (see Section 3.2):

$$\chi^2 = \sum_{i,j=1}^{N} \Delta w(\theta_i) \mathbf{C}_{ij}^{-1} \Delta w(\theta_j), \quad (20)$$

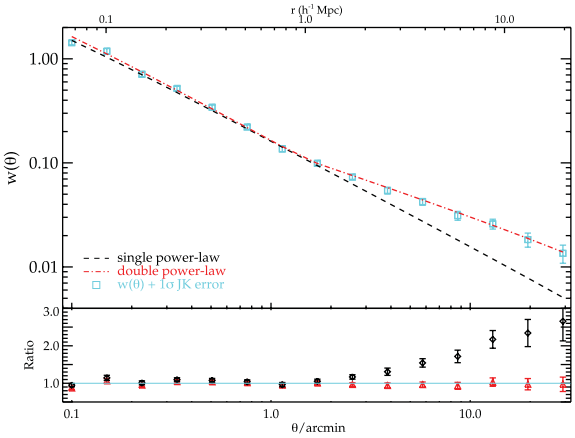

Figure 12. The best-fitting single power law (diamond) and double power law (triangle) for the 700 deg^{-2} LRGs candidates overplotted on the angular correlation function (square) with the 1σ Jackknife error. Lower panel shows the fitting residuals.

where N is the number of angular bins, $\Delta w(\theta_i)$ is the difference between the measured angular correlation function and the model for the ith bin, and $\mathbf{C}_{ij}^{-1}$ is the inverse of the covariance matrix.

For the single power law, our best-fitting spatial clustering length and clustering slope pair from Limber's formula are measured to be $r_0 = 7.54 \pm 0.16\,h^{-1}$ Mpc and $\gamma = 2.01 \pm 0.01$ with associated reduced $\chi^2_{red} = 5.89$. The $r_0 - \gamma$ pairs for the double power law are $r_{0,1} = 7.63 \pm 0.27\,h^{-1}$ Mpc and $\gamma_1 = 2.01 \pm 0.02$ at small scales and $r_{0,2} = 9.92 \pm 0.40\,h^{-1}$ Mpc and $\gamma_2 = 1.64 \pm 0.04$ at large scales with a reduced $\chi^2_{red} = 3.65$. From the intersection of the two power law for $\xi(r)$, we have calculated the break scale, $r_b = 2.38\,h^{-1}$ Mpc. This is higher than the $r_b = 1.3 - 2.2\,h^{-1}$ Mpc estimated from the SDSS, 2SLAQ and AAΩ LRG surveys (Sawangwit et al. 2011).

In Fig. 12 we show the data points including the 1σ Jackknife errors with the best-fitting power laws where the largest scale considered in the fitting was $\theta < 30$ arcmin, which corresponds to $r \lesssim 20\,h^{-1}$ Mpc at $z \sim 1$ for the 700 deg^{-2} LRG sample. Fig. 12 confirms that the double power law clearly gives a better fit to the data than the single power law. Note that in the case of the single power law and the double power law at small scales, our results give $r_0 - \gamma$ values consistent with outcomes from previous studies. However, at large scales the Stripe 82 slope ($\gamma_2 = 1.64 \pm 0.04$) is significantly flatter than the AAΩ result ($\gamma_2 = 1.81 \pm 0.02$).

Fig. 13 shows the double power-law fits for AAΩ (dashed red lines) taken from Sawangwit et al. and then evolved (black and green dot–dashed lines) to the Stripe 82 depth using equation (17) under the assumptions of comoving and virialized clustering, respectively. We shall interpret the amplitude scaling in the discussion of evolution in Section 6.1 later. At this point we again note that the biggest discrepancy seems to be at large scales where the Stripe 82 slope is increasingly too flat relative to the AAΩ result. Fitted parameters are given in Table 2, where the best-fitting power-law parameters for

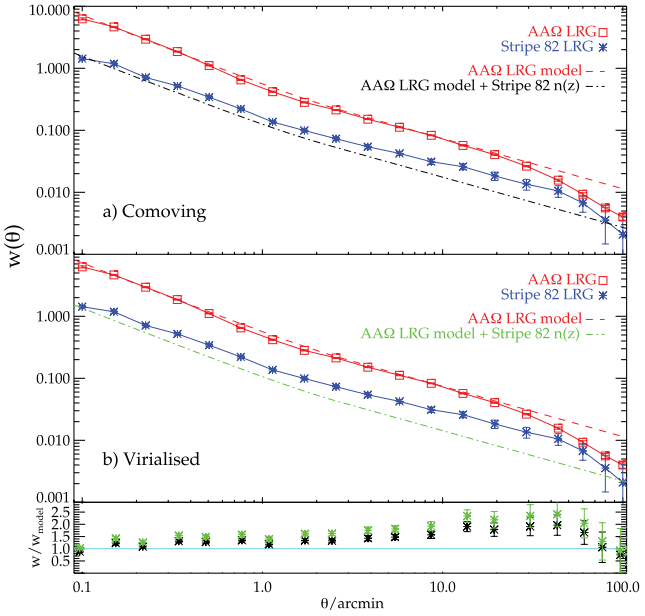

Figure 13. (a) The AAΩ LRG raw $w(\theta)$ measurements (red square) with predictions from comoving evolution model (dashed red line), using the best-fitting double power law $r_0 - \gamma$ values with Limber's formula as Sawangwit et al. (2011) calculated. We then evolve the AAΩ best-fits utilizing the estimated 700 deg^{-2} Stripe 82 LRG $n(z)$ under the assumption of comoving evolution (dash–dotted black line) clustering. The observed Stripe 82 LRG $w(\theta)$ is shown as well (blue star). (b) Same raw measurements as above, but now compared to the virialized evolution clustering model. Stripe 82 LRG $w(\theta)$ measurements are described more accurately with comoving evolution at small and large scales compared to virialized evolution as it can be seen from the lower panel where the residuals of the observed Stripe 82 $w(\theta)$ versus the comoving evolution (black star) and virialized evolution (green star) models are plotted, respectively.

the AAΩ LRG sample (Sawangwit et al. 2011) are also presented for comparison.

We note here that Kim et al. (2011) studied the clustering of extreme red objects (EROs) at $1 < z < 2$ in the SA22 field and they report a similar change of the large-scale slope. Gonzalez-Perez et al. (2011) tried to fit clustering predictions from semi-analytic simulations to the Kim et al. ERO $w(\theta)$ but found that the model underpredicts the clustering at large scales.

5.3 ΛCDM model fitting in the linear regime

Since the standard ΛCDM model was found to give a good fit to the lower redshift LRG samples of Sawangwit et al. (2011), we now check to see whether the flatter large-scale slope of the Stripe 82 LRG $w(\theta)$ leads to a statistically significant discrepancy with the ΛCDM model at $z \approx 1$. We generate matter power spectra using the 'CAMB' software (Lewis, Challinor & Lasenby 2000), including the case of non-linear growth of structure correction. For this reason we use the 'HALOFIT' routine (Smith et al. 2003) in 'CAMB'. Our models assume a ΛCDM Universe with $\Omega_\Lambda = 0.73$, $\Omega_m = 0.27$, $f_{baryon} = 0.167$, $\sigma_8 = 0.8$, $h = 0.7$ and $n_s = 0.95$. Then we transform the matter power spectra to obtain the matter correlation function, $\xi_m(r)$, using

$$\xi_m(r) = \frac{1}{2\pi^2} \int_0^\infty P_m(k) k^2 \frac{\sin kr}{kr} \, dk. \quad (21)$$

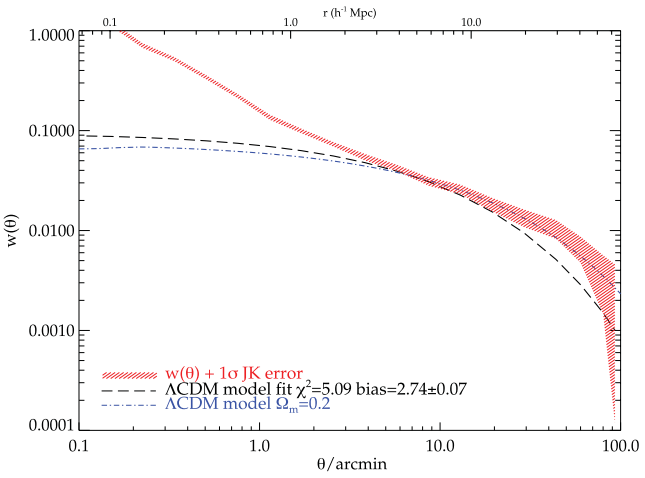

Figure 14. The best-fitting spatially flat ΛCDM model assuming $\Omega_m = 0.27$ compared to the observed $w(\theta)$ of Stripe 82 700 deg^{-2} LRGs in the linear regime. The standard model cannot explain the large-scale power excess in the angular correlation function of the Stripe 82 LRGs. The shaded area corresponds to $\pm 1\sigma$ jackknife error. Also shown is a spatially flat ΛCDM model with the same parameters as before except for a lower value of $\Omega_m = 0.2$ and an arbitrary normalization. The $\Omega_m = 0.2$ model appears to give a better fit than the standard $\Omega_m = 0.27$ model.

The relationship between the galaxy clustering and the underlying dark-matter clustering is given by the bias, b_g:

$$b_g^2(r) = \frac{\xi_g(r)}{\xi_m(r)}. \quad (22)$$

As we are interested in the linear regime, we fit the projected $\xi_m(r)$ to the Stripe 82 LRG $w(\theta)$ in the range $4 \lesssim \theta \lesssim 45$ arcmin, corresponding to comoving separations $3 \lesssim r \lesssim 30\,h^{-1}$ Mpc. By fitting the model predictions to the measured $w(\theta)$ it will result with the best linear bias factor, the only free parameter in this case. For our fitting, the χ^2-minimization with the full covariance matrix constructed from the jackknife resampling (see Section 3.2) has been used.

The best-fitting linear bias parameter is estimated to be $b = 2.74 \pm 0.07$ with $\chi^2_{red} = 5.09$. The upper limit of our fitted range in θ was varied, while the lower limit stayed constant to avoid any contribution from the non-linear regime. Thus, for the range ∼4–30 arcmin the best-fitting bias is $b = 2.8 \pm 0.08$ with $\chi^2_{red} = 4.72$ and at ∼ 4–60 arcmin it is $b = 2.69 \pm 0.07$ with $\chi^2_{red} = 5.18$. In Fig. 14 we plot the LRG $w(\theta)$ with the 1σ error and the ΛCDM model with the best-fitting bias. For low values of the upper limit of the fitting range, the measured biases are in approximate agreement with other results in the literature. But in terms of the flat slope of $w(\theta)$ at large scales, the standard ΛCDM linear model is inconsistent with the data at the 2–3σ level. One of the aims of the next section will be to see if an HOD model can explain the flat large-scale slope of the $z \approx 1$ Stripe 82 LRGs.

5.4 Halo model analysis

We are going to use the approach of the halo model (see Cooray & Sheth 2002, for a review) of galaxy clustering to finally fit our angular correlation function results. Under the halo-model framework we can examine the way the dark matter haloes are populated by galaxies through the HOD. Various studies have used this model to fit their results (e.g. Masjedi et al. 2006; White et al. 2007; Blake et al. 2008; Brown et al. 2008; Ross et al. 2008b; Wake et al.

2008; Zheng et al. 2009; Gonzalez-Perez et al. 2011; Sawangwit et al. 2011) as a way to explain the galaxy correlation function and gain insight into their evolution. Specifically, we shall investigate whether the HOD model may be able to explain the flatter slope of the correlation function observed here.

In the halo model, the clustering of galaxies is expressed by the contribution of number of pairs of galaxies within the same dark matter halo (one-halo term, $\xi 1$) and to pairs of galaxies in two separate haloes (two-halo term):

$$\xi(r) = \xi_{1h}(r) + \xi_{2h}(r). \tag{23}$$

The one-halo term dominates on small scales, $\lesssim$1 Mpc.

The fundamental ingredient in the HOD formalism of galaxy bias is the probability distribution $P(N|M)$, for the number of galaxies N hosted by a dark matter halo as a function of its mass M.

We use the so-called centre–satellite three-parameter HOD model (e.g. Seo et al. 2008; Wake et al. 2008; Sawangwit et al. 2011) which distinguishes between the central galaxy and the satellites in a halo. This separation has been shown in simulations (Kravtsov et al. 2004) and has been commonly used in semi-analytic galaxy formation models in the past years (Baugh 2006).

Different HODs are applied for the central and satellite galaxies. We assume that only haloes which host a central galaxy are able to host satellite galaxies. The fraction of haloes of mass M with centrals is modelled as

$$\langle N_c|M\rangle = \exp\left(\frac{-M_{min}}{M}\right). \tag{24}$$

In such haloes, the number of satellite galaxies follows a Poisson distribution (Kravtsov et al. 2004) with mean:

$$\langle N_s(M)\rangle = \left(\frac{M}{M_1}\right)^{\alpha}. \tag{25}$$

To describe the distribution of the satellite galaxies around the halo centre we use the NFW profile (Navarro, Frenk & White 1997). So, the mean number of galaxies residing in a halo of mass M is

$$\langle N|M\rangle = \langle N_c|M\rangle \times (1 + \langle N_s|M\rangle \tag{26}$$

and the predicted galaxy number density from the HOD is then

$$n_g = \int \mathrm{d}M\, n(M)\, \langle N|M\rangle \tag{27}$$

where $n(M)$ is the halo mass function, where in our case we use the model of Sheth & Lemson (1999).

From the HOD we can derive useful quantities which are the central fraction:

$$F_{cen} = \frac{\int \mathrm{d}M\, n(M)\, \langle N_c(M)\rangle}{\mathrm{d}M\, n(M)\, \langle N_c(M)\rangle\, [1 + \langle N_s(M)\rangle]}, \tag{28}$$

and the satellite fraction of the galaxy population:

$$F_{sat} = \frac{1}{n_g}\int \mathrm{d}M\, n(M)\, \langle N_c(M)\rangle\, \langle N_s|M\rangle\,, \tag{29}$$

as $F_{sat} = 1 - F_{cen}$. We can also determine the effective mass, M_{eff}, of the HOD:

$$M_{eff} = \frac{1}{n_g}\int \mathrm{d}M\, n(M) M\, \langle N|M\rangle\,, \tag{30}$$

and the effective large-scale bias:

$$b_g = \frac{1}{n_g}\int \mathrm{d}M\, n(M) b(M)\, \langle N|M\rangle\,, \tag{31}$$

where $b(M)$ is the halo bias, for which we use the ellipsoidal collapse model of Sheth, Mo & Tormen (2001) and the improved parameters of Tinker et al. (2005).

As the galaxy correlation function is the Fourier transform of the power spectrum, the one-halo term and the two-halo term of the clustering functions can be written as

$$P(k) = P_{1h}(k) + P_{2h}(k). \tag{32}$$

Moreover, the one-halo term can be distinguished from the contribution of the central–satellite pairs, $P_{cs}(k)$, and satellite–satellite pairs, $P_{ss}(k)$ (see e.g. Skibba & Sheth 2009):

$$P_{cs}(k) = \frac{1}{n_g^2}\int \mathrm{d}M\, n(M) 2\, \langle N_c|M\rangle\, \langle N_s|M\rangle\, u\, \langle k|M\rangle\,, \tag{33}$$

and

$$P_{ss}(k) = \frac{1}{n_g^2}\int \mathrm{d}M\, n(M)\, \langle N_c|M\rangle\, \langle N_s|M\rangle^2\, u\, \langle k|M\rangle^2\,, \tag{34}$$

where $u\,\langle \mathrm{k}\,|\,\mathrm{M}\rangle$ is the NFW density profile in Fourier space and we have simplified the number of satellite–satellite pairs $\langle N_s(N_s - 1)\,|\,M\rangle$ to $\langle N_s\,|\,M\rangle^2$ since the satellites are Poisson-distributed.

The two-halo term is evaluated as

$$P_{2h}(k, r) = P_m(k) \times \frac{1}{n_g'^2} \times \left[\int_0^{M_{lim}(r)} \mathrm{d}M\, n(M) b(M, r)\, \langle N(M)\rangle\, u(k, M)\right]^2, \tag{35}$$

where $P_m(k)$ is a non-linear matter power spectrum. We derive the mass limit, $M_{lim}(r)$, using the 'n_g'-matched' approximation of Tinker et al. (2005), which accounts the effect of halo exclusion: different haloes cannot overlap. n_g' is the restricted galaxy number density (equation B13 of Tinker et al. 2005).

For the scale-dependent halo bias, $b(M, r)$, we use the model given by Tinker et al. (2005):

$$b^2(M, r) = b^2(M)\frac{[1 + 1.17\xi_m(r)]^{1.49}}{[1 + 0.69\xi_m(r)]^{2.09}}, \tag{36}$$

where $\xi_m(r)$ is the non-linear matter correlation function. For the two-halo term, we need to correct the galaxy pairs from the restricted galaxy density to the entire galaxy population.

By using Limber's formula to project the predicted spatial galaxy correlation function $\xi(r)$ to the angular correlation function $w(\theta)$, we fit for a variety of the three-parameter halo model (M_{min}, M_1, α).

The best-fitting model for each of our sample is then determined from the minimum value of the χ^2-statistic using the full covariance matrix. We use the full covariance matrix over the range $0.25 < \theta <$ 60 arcmin in our fitting. Smaller scales are excluded in the fitting because any uncertainty in the $\xi(r)$ model can have a strong effect on $w(\theta)$ due to the projection. To determine the 1σ error on the fits, the region of parameter space from the best fits with $\delta\chi^2 \leq 1$ (1σ for 1 degree of freedom) is considered. For b_{lin}, M_{eff}, F_{sat} and n_g which depend on all the three main parameters, the considered region of the parameter space becomes $\delta\chi^2 \leq 3.53$.

Fig. 15(a) shows the resulting best-fitting HOD of the mean number of LRGs per halo along with the central and satellite contributions. The best-fitting values for M_{min}, M_1 and α were $M_{min} = 2.19 \pm 0.63 \times 10^{13}\, h^{-1}\, \mathrm{M}_\odot$, $M_1 = 21.9 \pm 5.6 \times 10^{13}\, h^{-1}\, \mathrm{M}_\odot$ and $\alpha = 2.24 \pm 0.12$, respectively. The associated values for b_{lin}, M_{eff}, F_{sat} and n_g are given in Table 3.

We see that the $\langle N\,|\,M\rangle$ of the LRGs flatten at unity, as expected from the assumption satellite galaxies are hosted by haloes with

Table 3. Best-fitting HOD parameters.

Sample	$\bar{z}$	$M_{\rm min}$ ($10^{13}\,h^{-1}\,{\rm M}_{\odot}$)	M_1 ($10^{13}\,h^{-1}\,{\rm M}_{\odot}$)	α	$n_{\rm g}$ ($10^{-4}\,h^3\,{\rm Mpc}^{-3}$)	$M_{\rm eff}$ ($10^{13}\,h^{-1}\,{\rm M}_{\odot}$)	$F_{\rm sat}$ (per cent)	$b_{\rm lin}$	$\chi^2_{\rm red}$
AAΩ	0.68	1.02 ± 0.03	12.6 ± 1.0	1.50 ± 0.03	3.1 ± 0.4	3.0 ± 0.1	9.0 ± 0.09	2.08 ± 0.03	13.6
Stripe 82 (10 arcmin)	1.0	3.09 ± 0.75	30.2 ± 6.7	2.38 ± 0.12	0.5 ± 0.3	4.0 ± 0.6	2.13 ± 1.0	3.01 ± 0.21	2.4
Stripe 82 (30 arcmin)	1.0	2.57 ± 0.31	25.7 ± 3.1	2.28 ± 0.04	0.6 ± 0.2	3.6 ± 0.5	2.62 ± 0.07	2.90 ± 0.15	2.3
Stripe 82 (45 arcmin)	1.0	2.19 ± 0.63	21.9 ± 5.6	2.24 ± 0.12	0.8 ± 0.3	3.3 ± 0.6	3.17 ± 0.10	2.81 ± 0.18	3.1
Stripe 82 (60 arcmin)	1.0	2.19 ± 0.21	21.9 ± 2.1	2.25 ± 0.05	0.8 ± 0.2	3.3 ± 0.3	3.17 ± 0.08	2.81 ± 0.10	3.6

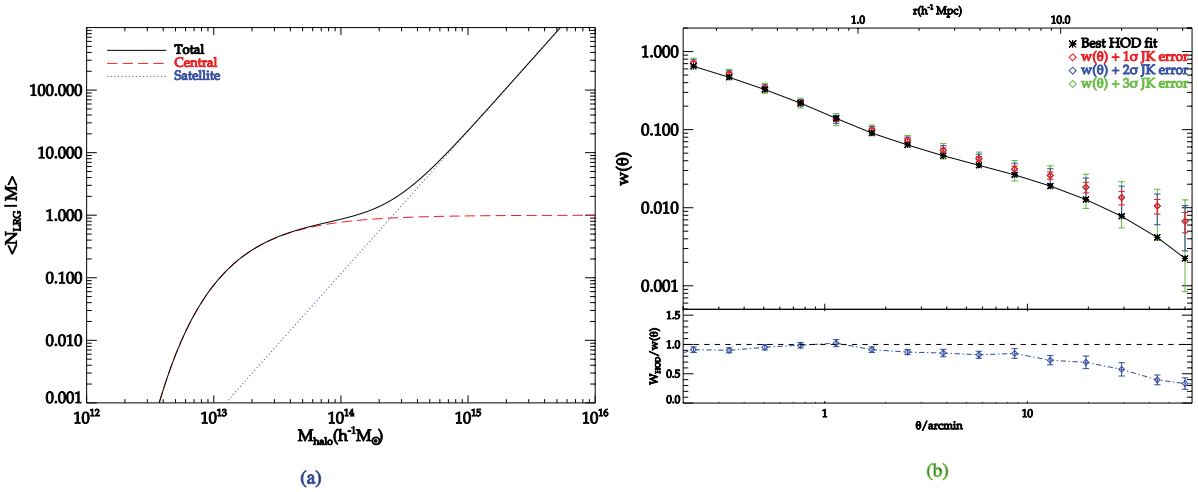

Figure 15. (a) The mean number of LRGs per halo as a function of halo mass at $z = 1$. The total, central and satellite contributions are shown by the solid, dashed and dotted lines, respectively. (b) The measured angular correlation function $w(\theta)$ for the 700 deg^{-2} LRG sample with the best HOD fit (black star). The 1, 2 and 3σ Jackknife errors are shown in red, blue and green, respectively.

central galaxies. The LRGs as expected populate massive dark matter haloes with the masses $\approx 10^{13}$–$10^{14}\,h^{-1}\,{\rm M}_{\odot}$. With the fraction of LRGs that are satellites being less than 5 per cent, we therefore find that >95 per cent of LRGs are central galaxies in their dark matter haloes. The best-fitting linear bias, $b_{\rm lin} \approx 2.8$, agrees with the prediction from Sawangwit et al. (2011) in the case of a long-lived model for the LRGs and indicates that the LRGs are highly biased tracers of the clustering pattern. The effective mass, $M_{\rm eff} \approx 3 \times 10^{13}\,h^{-1}\,{\rm M}_{\odot}$, confirms that LRGs are hosted by the most massive dark matter haloes. Despite the fact that we use a higher redshift LRG sample, our best-fitting HOD parameters are statistically not too dissimilar to those found in previous LRG studies (e.g. see Table 3).

In Fig. 15(b) we show the best-fitting model for $w(\theta)$, compared to the data. The first thing we notice is that while at small scales the best-fitting HOD are in good agreement with the $w(\theta)$ measurements, at large scales the model fits only at 2–3σ. The flatter slope at large scales is responsible for that and we still are not able to say if this can be explained by evolution in the linear regime or any kind of systematic effect. In Section 7 we will check systematic errors that could affect our results.

Moreover, due to the fact that the high value of the best fit reduced $\chi^2 = 3.1$, we also try to fit the HOD models at different scales by using four different maximum θ bins of the covariance matrix in our fits, which we present in Table 3. The fits at large scales did not improve and above 45 arcmin there was not any change in the best-fitting HOD measurements.

Considering the two-halo term in the HOD model, one can see that the bias in this regime is mostly scale-independent and the correction factor is in fact having the opposite effect on the slope. The scale-independent bias is simply the average of the halo bias, $b(M)$, weighted by the halo mass function and the mean number of galaxies hosted by the corresponding halo. One way to boost the large-scale amplitude is to increase $M_{\rm min}$ and therefore increase the mass range of the halo where most galaxies occupy and hence linear bias and amplitude of the two-halo term. However, to compensate for the increased numbers of satellite galaxies (and consequently small-scale clustering amplitude) one must also increase M_1, the mass at which a halo hosts one satellite galaxy on average. Moreover, in order to produce the overall flatter slope one needs to increase $M_1/M_{\rm min}$. However, this would still overpredict the clustering amplitude in the intermediate scales, $r \sim 5$–$10\,h^{-1}$ Mpc. Note that our best-fitting HOD gives $M_1/M_{\rm min} \approx 10$, consistent with previous results for lower redshift LRGs of Sawangwit et al. (2011) and Wake et al. (2008). However, as noted earlier including $w(\theta)$ bins at larger and larger scales does not change the best-fitting parameters which means that $M_1/M_{\rm min}$ also remains unchanged due to the reason discussed above. We therefore conclude that the HOD prescription in the framework of standard ΛCDM cannot explain the observed large-scale slope in $w(\theta)$ of the $z \approx 1$ LRG sample.

6 CLUSTERING EVOLUTION

6.1 Intermediate scales

First, we compare the clustering of the $z \approx 1$ Stripe 82 LRG sample to the lower redshift $z \approx 0.68$ AAΩ LRG sample. We recall that these LRG samples have approximately the same space density and so should be approximately comparable. We follow Sawangwit et al. (2011) and by using our best-fitting r_0 and γ we make comparison

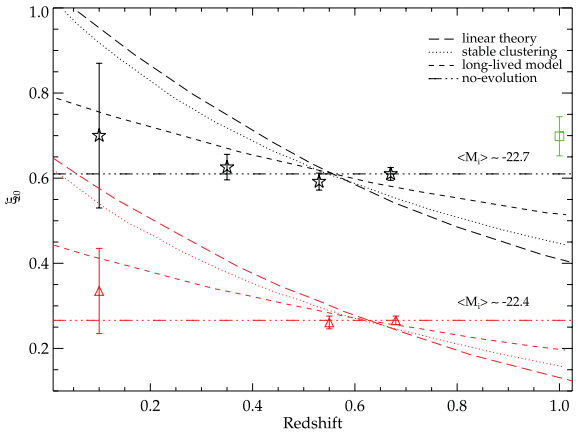

Figure 16. The LRG ξ_{20} measurements as a function of redshift and luminosity from Sawangwit et al. (2011). Lowest redshift data are early-type galaxies from 2dFGRS (Norberg et al. 2002). Stars represent the brighter samples (SDSS, 2SLAQ* and AA$\Omega^\star$-LRG), where the lower luminosity samples, triangles, have been lowered by 0.2 for clarity. The 700 deg^{-2} Stripe 82 LRGs ξ_{20} measurement is at $z = 1$ (square).

with their data and models via the integrated correlation function in a 20 h^{-1} Mpc sphere, ξ_{20}.

AAΩ LRG results are described better with the long-lived model of Fry (1996). Fry's model assumes no merging in the clustering evolution of the galaxies while they move within the gravitational potential, hence the comoving number density is kept constant. The bias evolution in such a model is given by

$$b(z) = 1 + \frac{b(0) - 1}{D(z)}, \tag{37}$$

where $D(z)$ is the linear growth factor.

However, the flat slope beyond 1 h^{-1} Mpc causes a highly significant, ≈50 per cent, rise in ξ_{20} above the AAΩ ξ_{20} as we can see in Fig. 16 [see also Figs 13(a) and (b)]. If we assume that the two samples are matched then we would conclude that all of the models discussed by Sawangwit et al. (2011) were rejected.

One possibility is that the 700 deg^{-2} LRG sample is closer to the SDSS and AA$\Omega^\star$ LRG space density of $1.1 \times 10^{-4}\, h^{-3}$ Mpc^{-3} because the LRG ξ_{20} fits the extrapolated models better there. If so, then this would imply that the Stripe 82 LRG $n(z)$ width was underestimated in the cross-correlation procedure and this would then increase the deprojected amplitude of $\xi(r)$, suggesting that this explanation may not work. Similarly a larger correction for stellar contamination would also produce a higher Stripe 82 clustering amplitude. We do not believe that looking further into the evolution of the bias (Papageorgiou et al. 2012) and DMH is warranted until we understand the flat slope of the Stripe 82 $w(\theta)$ at large scales.

6.2 Small scales

At smaller scales ($r < 1\, h^{-1}$ Mpc), the situation is less complicated by the flat large-scale slope. Here Sawangwit et al. found that a virialized model gave a better fit to the slightly faster evolution needed to fit the small-scale correlation function amplitudes than a comoving model. But in the present case, the scaling between the AAΩ and Stripe 82 LRGs in Figs 13(a) and (b) shows that here the comoving model is preferred at small scales over the faster virialized evolution. This fits with the more general picture of the Stripe 82 LRGs presenting a higher amplitude than expected all the way down to the smallest scales. Unfortunately, the remaining uncertainty in the Stripe 82 LRG luminosity class is still too large to make definitive conclusions on this evolution possible.

6.2.1 HOD evolution

Given the uncertainty in ξ_{20} caused by the flat $w(\theta)$ slope on intermediate–large scales, we will extend further the studies at small scales, using the HOD model to interpret the small-scale clustering signal of the LRGs. Based on the HOD fit at $z \approx 1$, we again follow Sawangwit et al. (2011) (and references therein) and test long-lived and merging models by comparing the predictions of these models to the SDSS HOD fit from Sawangwit et al. These authors and also Wake et al. (2008) found that long-lived models were more strongly rejected at small scales ($r < 1\, h^{-1}$ Mpc) than at intermediate–large scales.

Again we follow the approach of Wake et al. (2008)) and Sawangwit et al. (2011) who assumed a form for the conditional halo mass function (Sheth & Tormen 2002) and a sub-Poisson distribution for the number of central galaxies in low-redshift haloes of mass M such that

$$\langle N_{\rm c}(M)\rangle = 1 - \left[1 - \frac{C(M)}{N_{\rm max}}\right]^{N_{\rm max}}, \tag{38}$$

where $N_{\rm max} = {\rm int}(M/M_{\rm min})$,

$$C(M) = \int_0^M {\rm d}m\, N(m, M)\, \langle N_{\rm c}(m)\rangle \tag{39}$$

and $N(m, M)$ is the expression of Sheth & Tormen (2002) for the conditional halo mass which generalize those of Lacey & Cole (1993). The mean number of satellite galaxies in the low-redshift haloes is then given by

$$\langle N_{\rm c}(M)\rangle\, \langle N_{\rm s}(M)\rangle = S(M) + f_{\text{no-merge}}\, [C(M) - \langle N_{\rm c}(M)\rangle], \tag{40}$$

where

$$S(M) = \int_0^M {\rm d}m\, N(m, M)\, \langle N_{\rm c}(m)\rangle\, \langle N_{\rm s}(m)\rangle \tag{41}$$

and the main parameter is $f_{\text{no-merge}}$ which is the fraction of unmerged low-z satellite galaxies which were high-z central galaxies.

This model is called 'central–central mergers' in Wake et al. (2008). More massive high-z central galaxies are more likely to merge with one another or the new central galaxy rather than satellite-satellite mergers.

Setting $f_{\text{no-merge}} = 1$ means that there is no merging of initial central galaxies in subsequently merged haloes, so it is similar to the passive/long-lived model. $f_{\text{no-merge}}$ equal to 0 means that all the central galaxies in haloes at high redshift merge to form new central and/or satellite galaxies in the low-redshift haloes. In the analysis below, we use the best-fitting HOD model values as estimated for scales up to 45 arcmin (see Table 3).

The $f_{\text{no-merge}} = 1$ case is shown as the $w(\theta)$ passive model in Fig. 17 and is clearly rejected by the data at $\theta \lesssim 10$ arcmin (see lower panel). Best-fitting HOD predictions of the satellite fraction in the case of the passively evolved LRGs from $z_{\rm earlier} = 1$ to $z_{\rm later} = 0.35$ is $F_{\rm sat} = 18.6 \pm 2.5$ per cent whereas Sawangwit et al. measured $F_{\rm sat} = 18 \pm 1$ per cent for a brighter selection of LRGs at $z_{\rm earlier} = 0.68$. We see that both these results, for the long-lived model, are significantly higher compared to the best-fitting SDSS HOD, $F_{\rm sat} = 8.1 \pm 1.8$ per cent. The difference in the number of the satellite galaxies is explained as the predicted clustering amplitude at small scales (one-halo term) for the passive model is higher compared to the SDSS HOD fit as is clearly shown in Fig. 17. Higher clustering

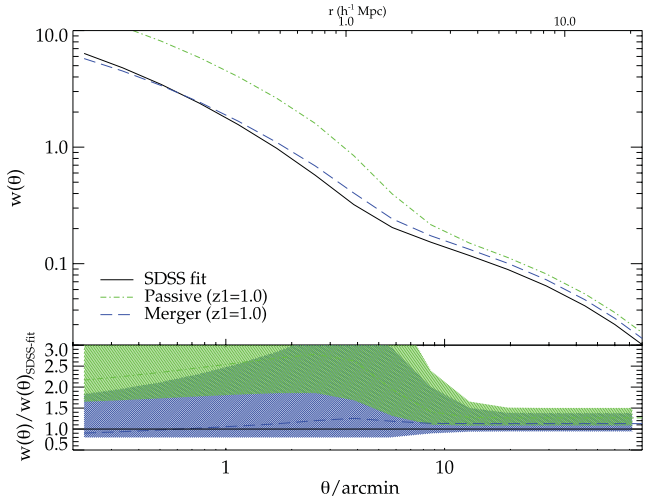

Figure 17. The predicted SDSS LRG $w(\theta)$s at $z_{\rm later} = 0.35$ for the case of passively ($f_{\rm no\text{-}merge} = 1$) evolving the best-fitting HOD of Stripe 82 LRGs sample from $z_{\rm earlier} = 1$ and the case where central galaxies' merging is allowed from $z_{\rm earlier} = 1$ ($f_{\rm no\text{-}merge} = 0.21$), in green dot–dashed line and blue long-dashed line, respectively. The bottom panel shows the ratios of the evolved $w(\theta)$s to the SDSS best fit; the shaded regions signify the 1σ uncertainties.

signal at small scales indicates the presence of too many satellite galaxies in the low-redshift haloes.

The $w(\theta)$ merger model is described by $f_{\rm no\text{-}merge} = 0.21$ as presented in Fig. 17 and clearly fits the data well. For this model the satellite fraction at $z = 0.35$ is estimated to be $F_{\rm sat} = 7.29 \pm 4.5$ per cent and is in good agreement with Sawangwit et al. Moreover, the best-fitting HOD model values for the evolved $z_{\rm earlier} = 1$ LRGs to $z_{\rm later} = 0.35$ for bias and galaxy number density are $b = 2.24 \pm 0.24$ and $n_{\rm g} = 0.67 \pm 0.41\ 10^{-4}\ h^3\ {\rm Mpc}^{-3}$, respectively. When the Stripe 82 best-fitting HOD model is compared to the SDSS best-fitting model, with $b = 2.08 \pm 0.05$ and $n_{\rm g} = 1.3 \pm 0.4\ 10^{-4}\ h^3\ {\rm Mpc}^{-3}$, the number of galaxies at $z = 0.35$ has decreased by almost 50 per cent due to central–central merging. The evolved linear bias and galaxy number density are consistent with the $z = 0.35$ best-fitting HOD of Sawangwit et al. at 1–1.5σ level.

Note that the agreement at large scales in Fig. 17 is somewhat artificial given the underestimation of $w(\theta)$ by the HOD model in Fig. 15(b) which remains unexplained in the HOD formalism. But at these smaller scales the result that the merging model fits better than the long-lived or indeed the virialized clustering model of Fig. 13(b) may be more robust, given the reasonable fit of the HOD model at small scales ($\theta < 3$ arcmin) in Fig. 15(b).

7 TESTS FOR SYSTEMATIC ERRORS

In this section we will present an extended series of checks for systematic errors that might have affected our clustering analysis, with the major issue being the flatter slope at large scales as estimated in Sections 5.2, 5.3 and 5.4. Tests for possible systematics that will be discussed here are as follows:

(i) data gradient artefacts,
(ii) $w(\theta)$ estimators bias,
(iii) survey completeness,
(iv) observational parameters, such as star density, galactic extinction, seeing, etc.

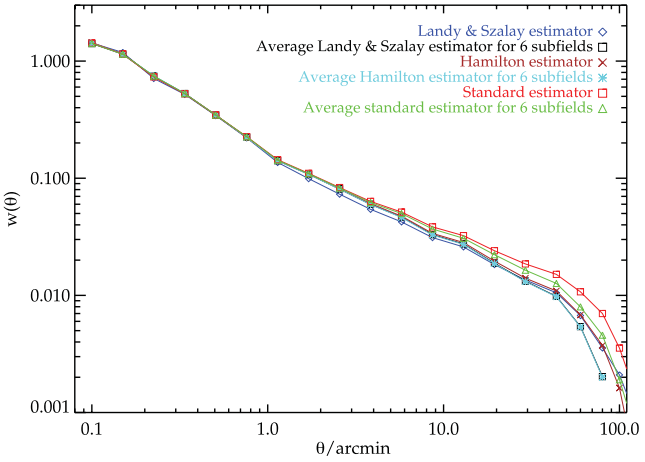

Figure 18. $w(\theta)$s from Landy–Szalay, Hamilton and standard estimator of the 700 deg^{-2} LRG sample. For comparison, the averaged $w(\theta)$s from the six subfields (see text for more detail) are overplotted as measured from each estimator. Landy & Szalay and Hamilton estimators give similar results for the average subfields and the full sample measurements, respectively. The standard estimator is more biased at larger scales.

7.1 Data gradients and $w(\theta)$ estimator bias

A false clustering signal at large scales can arise from artificial gradients in the data, as the correlation function is very sensitive to such factors. In attempting to explain the behaviour of the observed $w(\theta)$ at large scales, first we divide the LRG sample area in six equal subfields in RA. Then the angular correlation function of each subfield has been calculated using the Landy & Szalay, Hamilton and the Peebles estimator – the standard estimator. Furthermore, we average the $w(\theta)$ results of the six subfields as measured by each estimator and compare them with 700 deg^{-2} LRG $w(\theta)$ full sample results (see Fig. 18).

From these comparisons, it is clear that when we use the Landy & Szalay and Hamilton estimators, we do not find any significant difference in the amplitude of the measured $w(\theta)$ between the averaged subfields' or between the full samples' measurements. When the averaged $w(\theta)$ measurements are compared with those from the full sample, only a very slightly smaller clustering signal in the averaged $w(\theta)$s is seen, barely visible in Fig. 18. Furthermore, this is only the amount expected from the integral constraint (see Section 3.2) on $w(\theta)$, if the above Landy & Szalay estimate is assumed to apply in a single sub-field area. The standard estimator is known to be subject to larger statistical errors at large scales and here the signal is actually stronger when compared with the other two estimators.

Moreover, in Fig. 19 we display the results of the $w(\theta)$ measurements from the six subfields individually against the full sample measurements as estimated with the Landy & Szalay estimator in all cases. Even now we cannot see any major trend through the subfields' correlation function measurements, except possibly for the $15^0 \leq {\rm RA} \leq 30^0$ subfield which has a steeper slope at larger scales.

7.2 Magnitude incompleteness

Another issue that we want to address is how the clustering signal can be affected by magnitude incompleteness. The *izK* colour selection used for the LRGs is applied up to the faintest limits of the SDSS-UKIDSS LAS surveys (see Section 2.1). To account for this,

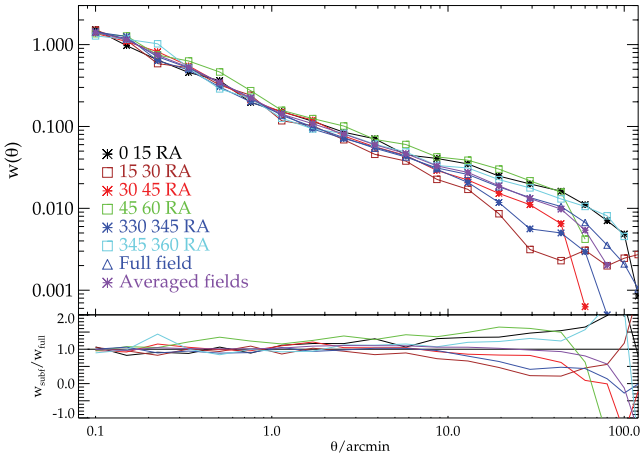

Figure 19. $w(\theta)$ results of the six equal-sized subfields ($15 \times 2.5\,\mathrm{deg}^2$ each) across Stripe 82, the total area as estimated by using the Landy–Szalay estimator and the averaged clustering signal from the six subfields. In the bottom panel are displayed the ratios of the $w(\theta)$ of each subfield compared to the total area.

Table 4. *K*-limited sub-samples used for auto-correlations in Fig. 20.

K	LRGs $700\,\mathrm{deg}^{-2}$
17.0–17.2	4894
17.2–17.4	11 096
17.4–17.6	22 490
17.6–17.8	38 659
17.8–18.0	53 680

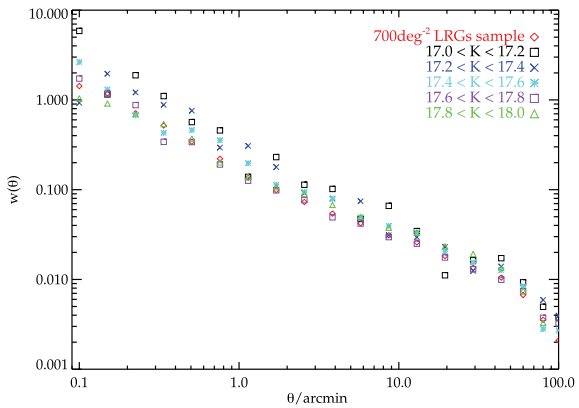

Figure 20. Auto-correlation functions from Landy–Szalay estimator for the $700\,\mathrm{deg}^{-2}$ LRG *K*-limited sub-samples from Table 4. Total sample is overplotted for comparison.

first we divide the $700\,\mathrm{deg}^{-2}$ LRG sample in 5 *K* magnitude bins in the range $17 < K < 18$. The number of LRGs in each magnitude bin is shown in Table 4.

Measurements of the angular correlation function from each *K* bin are shown in Fig. 20, where measurement uncertainties are not shown as we are mostly interested in the shape of the $w(\theta)$ in the linear regime. The clustering signal from the *K*-magnitude bins compared to the full sample does not show any significant difference at large scales and follows the full sample $w(\theta)$ shape. At smaller scales we see that the clustering from the brighter samples is higher than for the fainter samples, as expected.

The final tests of the magnitude incompleteness check are via the use of brighter colours in the *zK* selection. We therefore selected on the basis of brighter magnitudes down to $z \leq 21.2$ and $K \leq 17.2$ in various combinations and re-measured the angular correlation function. Even with these bright cuts, we did not see any change in the excess at large scales.

7.3 Observational parameters

The final test to identify a potential observational systematic effect follows the approach described by Ross et al. (2011), referring primarily to the area effectively masked by stars with magnitudes similar to the galaxies in the field. We cross-correlated the $700\,\mathrm{deg}^{-2}$ LRG sample with the Stripe 82 star catalogue from Ivezić et al. (2007) in four magnitude bins, $i < 19.5$, 20, 20.5, 21. From the measured autocorrelation function of stars and the cross-correlation function of stars with LRGs we computed the effect of stellar masking on the LRG correlation function using their equations (28) and (29). We show these results in Fig. 21(a).

The cross-correlation results show a very small anticorrelation between LRGs and stars for the $i = 19.5$ and 20.5 bins. A possible explanation for this anticorrelation might be related to the fact that we see an increase in the star number density between $330 \leq \mathrm{RA} \leq 340^\circ$ (see Fig. 21 b). Next, we calculate the expected $w(\theta)$, as defined in equation (29) of Ross et al. (2011). In all cases, there was little difference in the expected and observed $w(\theta)$ of the $700\,\mathrm{deg}^{-2}$ LRG sample. We conclude that the effect of stellar masking is essentially negligible, less than 1 per cent of the clustering signal at $\theta \approx 90$ arcmin.

There are other sources of possible systematics as well as star masking. Ross et al. (2011) also checked observational parameters such as galactic extinction, sky background, seeing and airmass using the cross-correlation technique. The Stripe 82 LRG sample is *K*-limited. Hence, we explore if the above observed parameters from the UKIDSS LAS *K* band could be sources of systematic errors at large scales. Fig. 22 displays the number density of Stripe 82 LRGs and how it is related with each potential observational systematic (stars are from Ivezić et al. 2007). From Fig. 22 we see a sharp decrease in the number of LRGs with high galactic extinction and poor seeing. The airmass fluctuations are also large compared to the error bars. The majority of the LRGs lie within the first few bins of galactic extinction, seeing and airmass in Fig. 22, but the LRGs in the rest of the bins with higher values could introduce systematics in the clustering signal.

Ho et al. (2012) present a method to identify which combination of the observed parameters could have the biggest effect on the clustering measurements. The authors in this work expressed the linear relationship between the potential observational systematic and its effect on the observed overdensity of galaxies, through the ϵ factor. In Fig. 23(a) we show the ϵ_i parameters for each of the observational parameters. The Ross et al. (2011) cross-correlation correction technique requires that ϵ be constant, so we use the best-fitting constant value of ϵ as calculated with the lowest chi-square fits from field-to-field errors. We find that the biggest correction in the angular correlation function is for the combined seeing, airmass and galactic extinction observational parameters (see equation 29 of Ross et al.). Also, a slightly smaller correction has been found for stars, sky background and galactic extinction. In Fig. 23(b) we show the original uncorrected $w(\theta)$ for the Stripe 82 LRGs, the $w(\theta)$ after applying the combined correction for the seeing, airmass and galactic extinction. In the same figure, for comparison we plot the best-fitting ΛCDM model as displayed in Fig. 14. So far, this

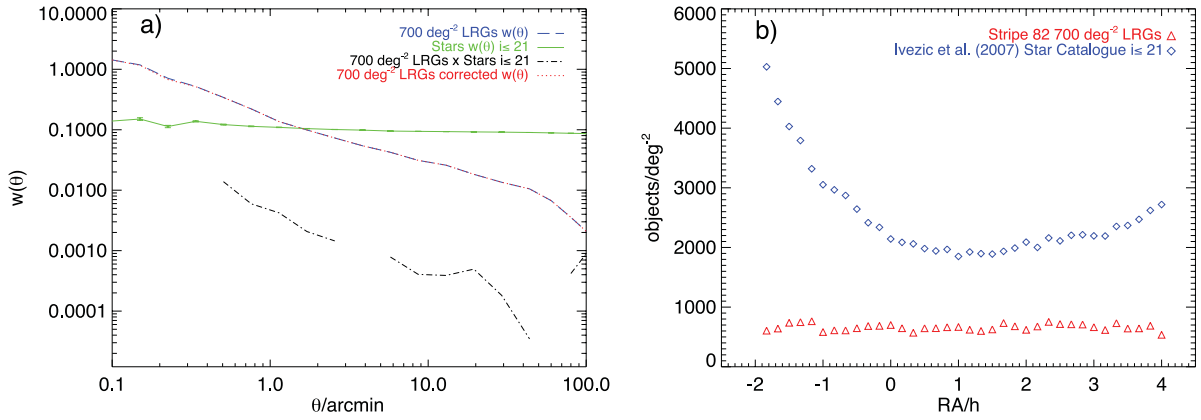

Figure 21. (a) The observed $w(\theta)$ of Stripe 82 LRGs (blue dashed line), Stripe 82 star catalogue of Ivezić et al. (2007) autocorrelation (green line) for $i \leq 21$, cross-correlations of the aforementioned LRGs stars (black dash–dotted line) and the resulted corrected observed autocorrelation function following Ross et al. (2011). We see that there is no difference between the observed LRGs and the corrected $w(\theta)$s, respectively. (b) The number density of the stars up to $i = 21$ from Ivezić et al. (2007) catalogue (blue diamonds) and the 700 deg^{-2} LRG sample (red triangles) across the Stripe 82. There is a strong gradient in the star distribution towards one end of the Stripe 82 at $330 \lesssim \mathrm{RA} \lesssim 340^\circ$ or $-2 \lesssim \mathrm{RA} \lesssim -1$ h in the abscissa notation. But when we excluded this area from the star–LRG cross-correlation, there was no change in the large-scale $w(\theta)$ signal.

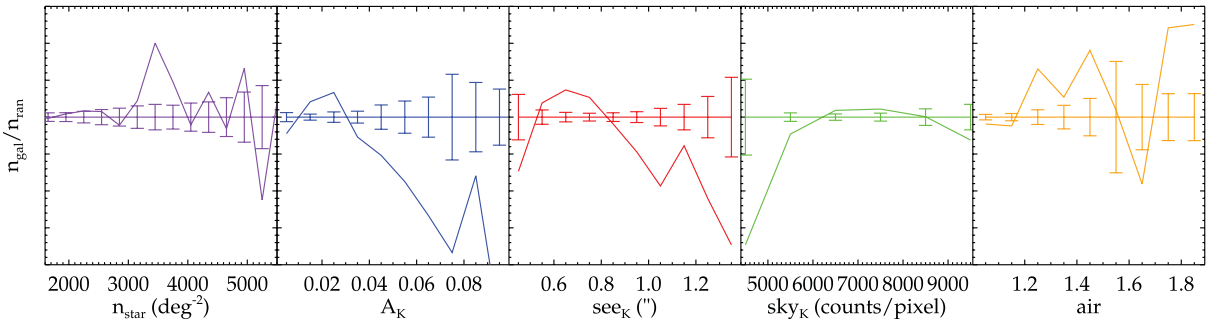

Figure 22. The projected number density of Stripe 82 LRGs as a function of the potential observable systematics: stellar density (n_{star}), Galactic extinction (A_k) in the K band, the K-band seeing (see_K), K-band background median sky flux in counts per pixel and the airmass (air). The errors are the standard deviation of the measurements within each bin.

correction in our $w(\theta)$ results is the most important. But still as we can see from Fig. 23(b), at the range 20–80 arcmin, the amplitude of the angular correlation function does not show the expected behaviour of the standard model. We have checked for the most common sources of systematics in the literature. Our data could still be affected by hidden artefacts, a case that future studies might be able to identify, but for the moment we will take the corrected result in Fig. 23(b) as our best estimate. Note that the HOD fits of Section 5.4 were only done up to $\theta \leq 60$ arcmin where there is little change in the form of our $w(\theta)$ result.

8 TEST FOR NON-GAUSSIANITY

One possible explanation for the flat slope seen at large scales is scale-dependent bias, although this is usually discussed more in the context of small-scale clustering. However, scale-dependent bias at large scales has previously been invoked to explain the discrepancy between the APM $w(\theta)$ results and $\Omega_{\mathrm{m}} = 1$ CDM models (Bower et al. 1993); in this case the scale dependence was caused by 'cooperative galaxy formation'.

Another possibility is that the LRG power spectrum may be closer to the primordial power spectrum at higher redshifts. But we have seen that the Stripe 82 clustering results are not in line with the standard ΛCDM model. These correlation function results are better fitted by a model with $\Omega_{\mathrm{m}} = 0.2$ rather than $\Omega_{\mathrm{m}} = 0.27$ (see Fig. 14), useful at least as an illustration of the size of the LRG clustering excess.

The third possibility is that the $z \approx 1$ LRG power spectrum may be better explained by scale-dependent bias at large scales due to primordial non-Gaussianity in the density fluctuations. The primordial non-Gaussianity of the local type is parametrized by $f_{\mathrm{NL}}^{\mathrm{local}}$ (see Bartolo et al. 2004, for a review) and is expected to contribute a $1/k^2$ term to the power spectrum and evolves as $\approx 1 + z$ (see equation 42). It is therefore best seen at large scales and high redshifts. Fig. 1 of Xia et al. (2010) shows the potential effect of non-Gaussianity on the biased clustering of radio sources with a similar redshift to the LRGs discussed here. It can be seen that the non-Gaussianity causes a strong positive tail to the correlation function for $\theta >$ a few degrees.

Xia et al. (2010), following Blake & Wall (2002), found that the NRAO VLA Sky Survey (NVSS) angular correlation function showed a strong positive tail suggesting that $f_{\mathrm{NL}}^{\mathrm{local}} = 62 \pm 27$. Xia et al. (2011) also inspected the angular correlation function of the DR6 1×10^6 QSO sample and found similar results to the radio sources with again an extended correlation function being seen implying similar values of f_{NL} (hereafter we shall use just f_{NL} to denote $f_{\mathrm{NL}}^{\mathrm{local}}$) as for the radio sources. This led to only slightly weaker constraints than for the radio sources in terms of the value of f_{NL}.

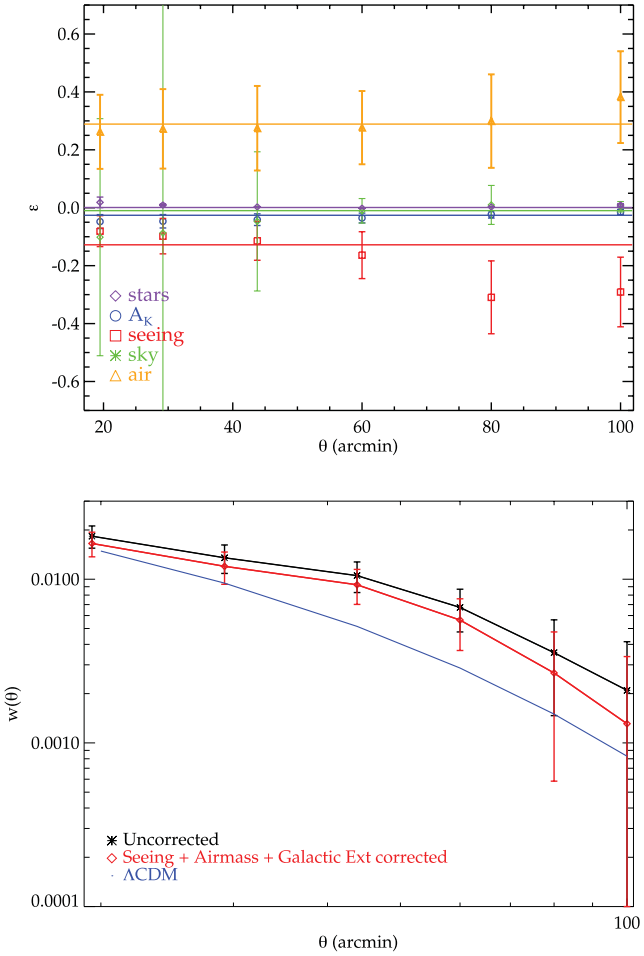

Figure 23. (a) Upper: similar to Ross et al. (2011) we plot ϵ, the linear factor between the potential observational systematic and its effect on the observed overdensity of galaxies for stars (purple diamond), galactic extinction (blue diamond), seeing (red squares), sky background (green diamond) and airmass (orange triangle). The solid lines are the best-fitting constant value of ϵ for each systematic. (b) Lower: the $w(\theta)$ measurement of the Stripe 82 LRGs without any cross-correlation correction (black star) and $w(\theta)$ corrected for seeing, airmass and galactic extinction combined (red diamond). The best-fitting ΛCDM model to the uncorrected measurement is plotted (blue line).

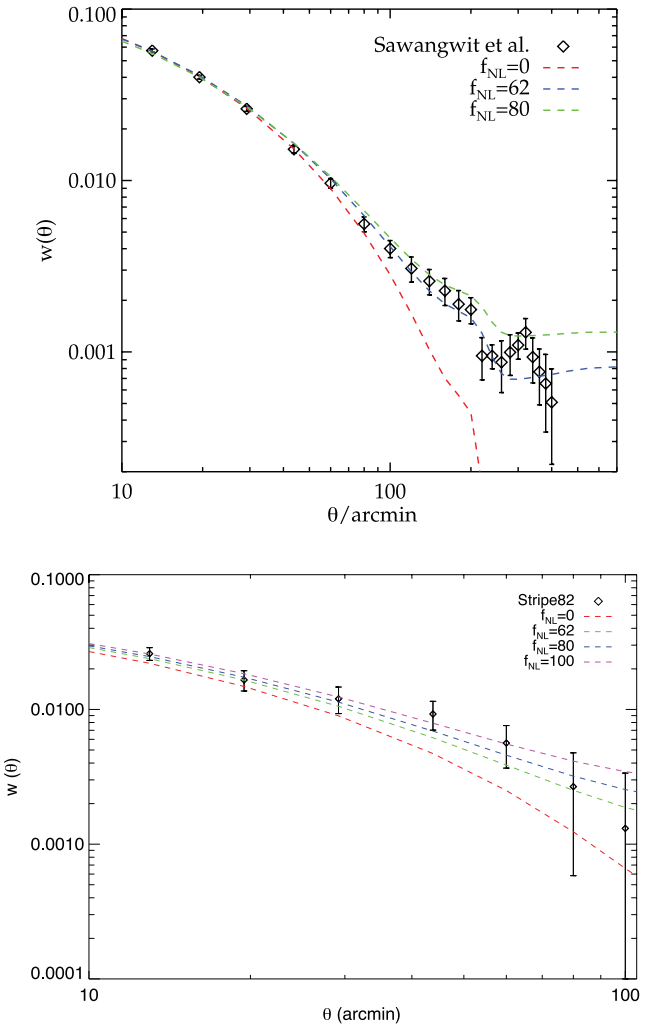

Figure 24. (a) Upper: the combined correlation function of Sawangwit et al. (2011) for the $z = 0.35$, $z = 0.55$ and $z = 0.68$ LRG samples, compared to a standard ΛCDM model ($f_{\rm NL} = 0$) and models with increasing degrees of primordial non-Gaussianity ($f_{\rm NL} = 62$, 80). (b) Lower: the Stripe 82 $z \approx 1$ LRG correlation function compared to a standard ΛCDM model ($f_{\rm nl} = 0$) and models with increasing degrees of primordial non-Gaussianity ($f_{\rm nl} = 62, 80, 100$).

Sawangwit et al. (2011) measured the combined angular correlation function of LRGs at $z \approx 0.35, 0.55, 0.68$ and found that although the results were in agreement with ΛCDM at scales $< 100\,{\rm h}^{-1}$ Mpc, at larger scales there was a possible excess, although this could still be due to systematics.

We then proceeded to follow Xia et al. and fit $f_{\rm NL}$ models. We use their relation between the non-Gaussian and Gaussian biases ($b_{\rm NG}$ and $b_{\rm G}$)

$$b_{\rm NG}(z) - b_{\rm G}(z) \simeq 2(b_{\rm G}(z) - 1) f_{\rm NL} \delta_{\rm ec}(z) \alpha_{\rm M}(k). \quad (42)$$

Here $\delta_{\rm ec}(z)$ is the critical density for ellipsoidal collapse and $\alpha_{\rm M}(k) \propto 1/k^2$ contains the scale and halo mass dependence (see Xia et al. for more details).

We first applied this relation to the case of the NVSS radio sources at $z \approx 0.7$. We found that adding the $1/k^2$ term to the standard cosmology $P(k)$ caused it to diverge and so we had to apply a large-scale cut-off, so that for $k < k_0$ then $P(k) = 0$. This is clearly a source of uncertainty in fitting for $f_{\rm NL}$. Nevertheless, we found that for $k_0 = 10^{-6}$, we could reproduce the results of Xia et al. (2010).

We then applied the same technique and cut-off to the combined AAΩ LRG and the Stripe 82 LRG $w(\theta)$s (after applying the combined correction for seeing, airmass and galactic extinction as estimated in Section 7.3). We first took the value of $b_{\rm G} = 2.08$ from the halo model fits of Sawangwit et al. (2011) and fitted for $f_{\rm NL}$. The result is shown in Fig. 24(a). We find that for AAΩ LRGs, the results for $f_{\rm NL}$ are reasonably compatible with those from the NVSS catalogue with values of $f_{\rm NL} = 60$–80 giving a better fit to the data in the range $1.5 < \theta < 6.^{\circ}5$.

The prediction from non-Gaussianity is that the large-scale slope will further flatten with redshift. We therefore compared the Stripe 82 LRGs to models with the same $f_{\rm NL}$ values and find no inconsistency (see Fig. 24b). Clearly the errors at the largest scales are more significant for the Stripe 82 data than for the AAΩ LRGs or the NVSS radio sources. However, the predicted flattening of the Stripe 82 correlation function at $\theta \approx 1^{\circ}$ makes the non-Gaussian

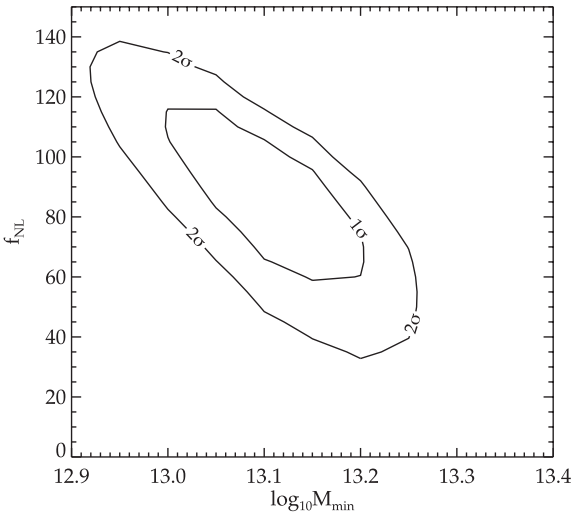

Figure 25. The minimum χ^2 is 5.5 over 11 d.o.f and the best-fitting parameters are $f_{NL} = 90 \pm 30$ (1σ) and $M_{min} = 1.26 \pm 0.22 \times 10^{13}\,h^{-1}\,M_\odot$. The best-fitting M_{min} here is lower than the full HOD fit assuming $f_{NL} = 0$ at $2.2 \times 10^{13}\,h^{-1}\,M_\odot$.

models more consistent with the data in this smaller angular range than the $f_{NL} = 0$ model. At larger scales the errors are larger and the data are therefore more in agreement with the standard model.

Fig. 25 shows the effect of jointly fitting f_{NL} on the minimum halo mass, M_{min}, in the HOD model. The best-fitting model now gives $M_{min} = (1.26 \pm 0.22) \times 10^{13} h^{-1}\,M_\odot$ and $f_{NL} = 90 \pm 30$, lower than the $M_{min} = 2.2 \times 10^{13}\,h^{-1}\,M_\odot$ value when $f_{nl} = 0$ is assumed in the full HOD fit.

We should say that rather than detections of non-Gaussianity, the present AAΩ and Stripe 82 LRG results should be more regarded as upper limits on non-Gaussianity. Large-scale angular correlation function results are still susceptible to large-scale gradients and even though there is no direct evidence for these in the AAΩ or Stripe 82 samples, there is still the possibility that these exist in the data. On the other hand, the classic test for the reality of a correlation function feature is that it scales correctly with depth and at least the SDSS and Stripe 82 LRG correlation functions in Figs 24(a) and (b) look like as they do so. It will be interesting to see if as QSO surveys (Sawangwit et al. 2012) and $z \approx 3$ LBG surveys (Bielby et al. 2012) grow, whether the correlation functions at higher redshift also show an increased slope flattening as predicted for the non-Gaussian models.

The other uncertainty that has arisen is in the non-Gaussian model itself where we have found that there is a rather strong dependence on a small-scale cut-off, k_0. Other authors have made some reference to this problem but only implicitly. It will be interesting to see if more accurate models for non-Gaussianity can numerically predict this cut-off from first principles.

9 SUMMARY AND CONCLUSIONS

We have measured $w(\theta)$ for ≈130 000 colour-selected galaxies in Stripe 82 exploiting SDSS DR7 $i + z$ bands and UKIDSS LAS K photometry. We used the cross-correlation technique of Newman (2008) to establish that the average redshift of the LRGs is $z \approx 1$. This sample therefore probes higher redshifts than the previous SDSS LRG samples of Sawangwit et al. (2011). We have established that a sample with sky density ≈700 deg^{-2} has a comparable space density to the $z \approx 0.68$ AAΩ LRG sample of Sawangwit et al. (2011). However, this is only an approximate correspondence which makes evolutionary comparisons between the redshifts more tricky. What is clear is that the $z \approx 1$ LRGs generally have a relatively high clustering amplitude. Compared to the AAΩ LRG $w(\theta)$ scaled to the depth of the Stripe 82 LRGs, the Stripe 82 $w(\theta)$ is higher at all scales, even those below $<1\,h^{-1}$ Mpc. Thus at intermediate scales, the $z \approx 1$ LRGs are not only more clustered than predicted by the long-lived evolutionary model, they are also more clustered than the comoving model. At small separations ($\lesssim 1\,h^{-1}$ Mpc) the correlation function amplitude is again somewhat higher than the AAΩ results scaled by the previously preferred stable clustering model. The Stripe 82 $w(\theta)$ also shows a very flat slope at large scales which means that the ΛCDM linear model has become a poorer fit than at lower redshift.

Partly to look for an explanation for the flat large-scale slope, we then fitted an HOD model to the Stripe 82 $w(\theta)$. The best-fitting parameters were $M_{min} = 2.19 \pm 0.63 \times 10^{13}\,h^{-1}\,M_\odot$, $M_1 = 21.9 \pm 5.6 \times 10^{13}\,h^{-1}\,M_\odot$, $b_{lin} = 2.81 \pm 0.18$, $M_{eff} = 3.3 \pm 0.6 \times 10^{13}\,h^{-1}\,M_\odot$, $F_{sat} = 3.17 \pm 0.08$ per cent and $n_g = 0.8 \pm 0.3 \times 10^{-4}\,h^3\,\mathrm{Mpc}^{-3}$. The high amplitude of the correlation function clearly pushes the halo masses up and the space densities down. The lowest chi-square fits were found when large scales were excluded but the reduced chi-squares were still in the range 2.3–3.6. This is actually an improvement over the lower redshift samples but this is certainly due to the larger errors on the Stripe 82 data. We conclude that it is not possible to find an explanation for the flat slope in the Stripe 82 $w(\theta)$ on the basis of the HOD model.

We also then studied the evolution of the HOD between $z = 1$ and $z = 0.35$. Similarly to that of Sawangwit et al. (2011), we concluded that a pure passive model with a low merger rate might produce too steep a $w(\theta)$ slope at small scales ($<1\,h^{-1}$ Mpc). In this case, we have already noted that the small-scale amplitude may also be too high for a passive model with stable clustering.

We have looked for an explanation of the flat slope in terms of systematics by cross-correlating the Stripe 82 LRG sample with stellar density, airmass, seeing, sky background and galactic extinction and used the method of Ross et al. (2011) to correct our $w(\theta)$. Even the combined correction for seeing, airmass and galactic extinction only produced a small change in $w(\theta)$ at large scales.

We conclude that the high amplitude and flat slope of the Stripe 82 LRGs $w(\theta)$ may have significant contributions from the uncertainty in the comparison between AAΩ and Stripe 82 LRG luminosities. However, this leaves a similar contribution from a new and unknown source. We have discussed large-scale, primordial, non-Gaussianity as one possibility for the source of this large-scale excess. We have suggested that the evidence from the AAΩ sample itself for an excess at even larger scales may fit in with the behaviour expected from non-Gaussianity over this redshift range. In this case we returned to the fitting of halo masses including the non-Gaussian component and found that the best fit M_{min} decreased from $2.2 \times 10^{13}\,M_\odot$ to $1.3 \times 10^{13}\,M_\odot$. More importantly, if the Stripe 82 large-scale $w(\theta)$ excess proves reliable and not due to systematics, then we have made a significant detection of non-Gaussianity in the $z \approx 1$ LRG distribution with an estimated local non-Gaussianity parameter estimate of $f_{NL}^{local} = 90 \pm 30$. This represents a 3σ detection at a level comparable to the present upper limit from *Wilkinson Microwave Anisotropy Probe* cosmic microwave background measurements of $f_{NL}^{local} = 32 \pm 21$ (Komatsu 2010).

ACKNOWLEDGMENTS

NN acknowledges receipt of a fellowship funded by the European Commission's Framework Programme 6, through the Marie Curie Early Stage Training project MEST-CT-2005-021074. US acknowledges financial support from the Institute for the Promotion of Teaching Science and Technology (IPST) of The Royal Thai Government.

We would like to thank Dr Nigel Hambly and the WSA-support team for their help with UKIDSS data. The UKIDSS project is defined in Lawrence et al. (2007). UKIDSS uses the UKIRT Wide Field Camera (WFCAM; Casali et al. 2007) and a photometric system described in Hewett et al 2006. The pipeline processing and science archive are described in Irwin et al. (2008) and Hambly et al. (2008).

Funding for the SDSS and SDSS-II has been provided by the Alfred P. Sloan Foundation, the Participating Institutions, the National Science Foundation, the U.S. Department of Energy, the National Aeronautics and Space Administration, the Japanese Monbukagakusho, the Max Planck Society, and the Higher Education Funding Council for England. The SDSS Web Site is http://www.sdss.org/.

The SDSS is managed by the Astrophysical Research Consortium for the Participating Institutions. The Participating Institutions are the American Museum of Natural History, Astrophysical Institute Potsdam, University of Basel, University of Cambridge, Case Western Reserve University, University of Chicago, Drexel University, Fermilab, the Institute for Advanced Study, the Japan Participation Group, Johns Hopkins University, the Joint Institute for Nuclear Astrophysics, the Kavli Institute for Particle Astrophysics and Cosmology, the Korean Scientist Group, the Chinese Academy of Sciences (LAMOST), Los Alamos National Laboratory, the Max-Planck-Institute for Astronomy (MPIA), the Max-Planck-Institute for Astrophysics (MPA), New Mexico State University, Ohio State University, University of Pittsburgh, University of Portsmouth, Princeton University, the United States Naval Observatory and the University of Washington.

Funding for the DEEP2 survey has been provided by NSF grants AST95-09298, AST-0071048, AST-0071198, AST-0507428 and AST-0507483 as well as NASA Long Term Space Astrophysics (LTSA) grant NNG04GC89G.

REFERENCES

Abazajian K. N. et al., 2009, ApJS, 182, 543
Bartolo N., Komatsu E., Matarrese S., Riotto A., 2004, Phys. Rev., 402, 103
Baugh C. M., 2006, Rep. Progress Phys., 69, 3101
Berlind A. A., Weinberg D. H., 2002, ApJ, 575, 587
Bielby R. et al., 2012, preprint (arXiv:1204.3635)
Blake C., Wall J., 2002, MNRAS, 337, 993
Blake C., Collister A., Lahav O., 2008, MNRAS, 385, 1257
Bower R. G., Coles P., Frenk C. S., White S. D. M., 1993, ApJ, 405, 403
Brown M. J. I. et al., 2008, ApJ, 682, 937
Bruzual G., Charlot S., 2003, MNRAS, 344, 1000
Cannon R. et al., 2006, MNRAS, 372, 425
Collister A. et al., 2007, MNRAS, 375, 68
Cooray A., Sheth R., 2002, Phys. Rev., 372, 1
Crocce M., Gaztañaga E., Cabré A., Carnero A., Sánchez E., 2011, MNRAS, 417, 2577
Davis M. et al., 2003, in Guhathakurta P., ed., Science Objectives and Early Results of the DEEP2 Redshift Survey, Proc. SPIE Vol. 4834, p. 161
Davis M. et al., 2007, ApJ, 660, L1
Eisenstein D. J. et al., 2001, AJ, 122, 2267
Eisenstein D. J. et al., 2003, ApJ, 585, 694
Fry J. N., 1996, ApJ, 461, L65
Fukugita M., Ichikawa T., Gunn J. E., Doi M., Shimasaku K., Schneider D. P., 1996, AJ, 111, 1748
Gonzalez-Perez V., Baugh C. M., Lacey C. G., Kim J.-W., 2011, MNRAS, 417, 517
Groth E. J., Peebles P. J. E., 1977, ApJ, 217, 385
Guo H., Zehavi I., Zheng Z., 2012, ApJ, 756, 127
Hamilton A. J. S., 1993, ApJ, 417, 19
Ho S. et al., 2012, ApJ, 761, 14
Ivezić Ž. et al., 2007, AJ, 134, 973
Jing Y. P., Mo H. J., Boerner G., 1998, ApJ, 494, 1
Kim J.-W., Edge A. C., Wake D. A., Stott J. P., 2011, MNRAS, 410, 24
Komatsu E., 2010, Classical and Quantum Gravity, 27, 124010
Kravtsov A. V., Berlind A. A., Wechsler R. H., Klypin A. A., Gottlöber S., Allgood B., Primack J. R., 2004, ApJ, 609, 35
Lacey C., Cole S., 1993, MNRAS, 262, 627
Landy S. D., Szalay A. S., 1993, ApJ, 412, 64
Lawrence A. et al., 2007, MNRAS, 379, 1599
Lewis A., Challinor A., Lasenby A., 2000, ApJ, 538, 473
Limber D. N., 1953, ApJ, 117, 134
Loh Y.-S., Strauss M. A., 2006, MNRAS, 366, 373
Lupton R., Gunn J. E., Ivezić Z., Knapp G. R., Kent S., Yasuda N., 2001, in Harnden F. R., Primini F. A., Payne H. E., eds, The SDSS Imaging Pipelines, ASP Conf. Ser. 238, Astron. Soc. Pac., San Francisco, p. 269
Ma C.-P., Fry J. N., 2000, ApJ, 543, 503
Masjedi M. et al., 2006, ApJ, 644, 54
Moore A. W. et al., 2001, in Banday A. J., Zaroubi S., Bartelmann M., eds, Mining the Sky, Proceedings of the MPA/ESO/MPE Workshop Held at Garching, Germany, July 31–August 4, 2000, p. 71
Myers A. D., Brunner R. J., Nichol R. C., Richards G. T., Schneider D. P., Bahcall N. A., 2007, ApJ, 658, 85
Navarro J. F., Frenk C. S., White S. D. M., 1997, ApJ, 490, 493
Newman J. A., 2008, ApJ, 684, 88
Norberg P. et al., 2002, MNRAS, 336, 907
Norberg P., Baugh C. M., Gaztañaga E., Croton D. J., 2009, MNRAS, 396, 19
Padmanabhan N. et al., 2007, MNRAS, 378, 852
Papageorgiou A., Plionis M., Basilakos S., Ragone-Figueroa C., 2012, MNRAS, 422, 106
Peacock J. A., Smith R. E., 2000, MNRAS, 318, 1144
Peebles P. J. E., 1980, The Large-scale Structure of the Universe. Princeton Univ. Press, Princeton, NJ
Richards G. T. et al., 2009, ApJS, 180, 67
Roche N., Eales S. A., 1999, MNRAS, 307, 703
Ross A. J., Brunner R. J., 2009, MNRAS, 399, 878
Ross N. P. et al., 2007, MNRAS, 381, 573
Ross N. P., Shanks T., Cannon R. D., Wake D. A., Sharp R. G., Croom S. M., Peacock J. A., 2008a, MNRAS, 387, 1323
Ross A. J., Brunner R. J., Myers A. D., 2008b, ApJ, 682, 737
Ross A. J., Percival W. J., Brunner R. J., 2010, MNRAS, 407, 420
Ross A. J. et al., 2011, MNRAS, 417, 1350
Sawangwit U., Shanks T., Abdalla F. B., Cannon R. D., Croom S. M., Edge A. C., Ross N. P., Wake D. A., 2011, MNRAS, 416, 3033
Sawangwit U., Shanks T., Croom S. M., Drinkwater M. J., Fine S., Parkinson D., Ross N. P., 2012, MNRAS, 420, 1916
Schlegel D. J., Finkbeiner D. P., Davis M., 1998, ApJ, 500, 525
Schneider D. P. et al., 2010, AJ, 139, 2360
Scoccimarro R., Sheth R. K., Hui L., Jain B., 2001, ApJ, 546, 20
Scranton R. et al., 2002, ApJ, 579, 48
Seljak U., 2000, MNRAS, 318, 203
Seo H.-J., Eisenstein D. J., Zehavi I., 2008, ApJ, 681, 998
Shanks T., Bean A. J., Ellis R. S., Fong R., Efstathiou G., Peterson B. A., 1983, ApJ, 274, 529
Sheth R. K., Lemson G., 1999, MNRAS, 304, 767
Sheth R. K., Tormen G., 2002, MNRAS, 329, 61
Sheth R. K., Mo H. J., Tormen G., 2001, MNRAS, 323, 1

Skibba R. A., Sheth R. K., 2009, MNRAS, 392, 1080
Smith J. A. et al., 2002, AJ, 123, 2121
Smith R. E. et al., 2003, MNRAS, 341, 1311
Tinker J. L., Weinberg D. H., Zheng Z., Zehavi I., 2005, ApJ, 631, 41
Wake D. A. et al., 2006, MNRAS, 372, 537
Wake D. A., Croom S. M., Sadler E. M., Johnston H. M., 2008, MNRAS, 391, 1674
Warren S. J. et al., 2007, MNRAS, 375, 213
White M., Zheng Z., Brown M. J. I., Dey A., Jannuzi B. T., 2007, ApJ, 655, L69
Xia J.-Q., Viel M., Baccigalupi C., De Zotti G., Matarrese S., Verde L., 2010, ApJ, 717, L17
Xia J.-Q., Baccigalupi C., Matarrese S., Verde L., Viel M., 2011, J. Cosmol. Astropart. Phys., 8, 33
Zehavi I. et al., 2005a, ApJ, 621, 22
Zehavi I. et al., 2005b, ApJ, 630, 1
Zheng Z., Zehavi I., Eisenstein D. J., Weinberg D. H., Jing Y. P., 2009, ApJ, 707, 554

This paper has been typeset from a TEX/LATEX file prepared by the author.